

Topological chiral currents in the Gross-Neveu model extension

E. Tirrito,¹ M. Lewenstein,^{2,3} and A. Bermudez^{4,5}

¹*International School for Advanced Studies (SISSA), via Bonomea 265, 34136 Trieste, Italy*

²*ICFO - Institut de Ciències Fotòniques, The Barcelona Institute of Science and Technology, Av. Carl Friedrich Gauss 3, 08860 Castelldefels (Barcelona), Spain*

³*ICREA, Lluís Companys 23, 08010 Barcelona, Spain*

⁴*Departamento de Física Teórica, Universidad Complutense, 28040 Madrid, Spain*

⁵*Instituto de Física Teórica, UAM-CSIC, Universidad Autónoma de Madrid, Cantoblanco, 28049 Madrid, Spain.*

We unveil an interesting connection of Lorentz-violating quantum field theories, studied in the context of the standard model extension, and Hubbard-type models of topological crystalline phases. These models can be interpreted as a regularisation of the former and, as hereby discussed, explored with current quantum simulators based on ultra-cold atoms in optical Raman lattices. In particular, we present a complete analysis of the Creutz-Hubbard ladder under a generic magnetic flux, which regularises a Gross-Neveu model extension, and presents a characteristic circulating chiral current whose non-zero value arises from a specific violation of Lorentz invariance. We present a complete phase diagram with trivial insulators, ferromagnetic and anti-ferromagnetic phases, and current-carrying topological crystalline phases. These predictions are benchmarked using tools from condensed matter and quantum-information science, showing that self-consistent Hartree-Fock and strong-coupling Dzyaloshinskii-Moriya methods capture the essence of the phase diagram in different regimes, which is further explored using extensive numerical simulations based on matrix-product states.

CONTENTS

I. Introduction	1
II. The Creutz-Hubbard ladder with arbitrary flux	3
A. Previous studies on Hubbard ladders	3
B. The synthetic Creutz-Hubbard ladder	4
C. Summary of the results	5
III. The Gross-Neveu model extension in the continuum limit	7
IV. Chiral currents and critical phenomena	9
A. Chiral flows and topological phase transitions	9
B. Dzyaloshinskii-Moriya super-exchange	11
V. Phase diagram: self-consistent Hartree-Fock method and variational matrix-product states	13
A. Weak and intermediate interactions	15
B. Strong Interactions	18
C. Entanglement spectroscopy	19
VI. Cold-atom Raman lattice scheme	21
VII. Conclusions and outlook	25
Acknowledgements	25
A. Weak interactions and coupled Ising chains	25
References	26

I. INTRODUCTION

The standard model (SM) of particle physics is one of the big triumphs of theoretical physics, as it provides simultaneously an accurate and economic description of nature [1]. The

SM introduces a reduced set of quantum fields and, building upon elegant and simple symmetry principles, it fixes the form of their interactions and precisely accounts for all fundamental particles observed to date. However, existing difficulties in the incorporation of gravity to the SM suggest that this model could be a low-energy limit of a more fundamental theory that describes physics at a much higher scale, the Planck scale. In these theories, fundamental symmetries such as Lorentz invariance may be broken, as occurs in string theory [2] and non-commutative field theories [3]. The remnants of this *Lorentz violation* can be included in the so-called standard model extension, an effective quantum field theory (QFT) in a larger parameter space that includes all possible Lorentz-violating terms with new bare couplings [4–6]. A wide variety of experiments [7], including recent quantum-information-enhanced interferometry [8], establish tight bounds on these couplings and, so far, have shown no evidence of the violation of Lorentz symmetry.

There is, however, an alternative arena where Lorentz invariance is not an exact symmetry but, instead, appears in the infrared long-wavelength limit [9]. In condensed-matter physics, many microscopic theories are formulated in terms of non-relativistic quantum field theories [10] and, yet, Lorentz invariance and relativistic effects can appear in effective descriptions of low-energy phenomena. The standard scenario where this happens is that of phase transitions [11], where the physics around some critical points can be described by Lorentz-invariant QFTs, and the renormalization group allows to understand why Lorentz-breaking microscopic corrections become irrelevant at low energies [12, 13]. Indeed, the dialogue between condensed matter and high-energy physics has proved to be extremely fruitful in this context, see e.g. [14] and [15, 16], or [17] and [18, 19]. An alternative scenario where the emergence of Lorentz invariance has turned out to be relevant is in graphene [20], Weyl semi-metals [21] and topological insulators and superconductors [22].

In recent years, this fertile dialogue has broadened its

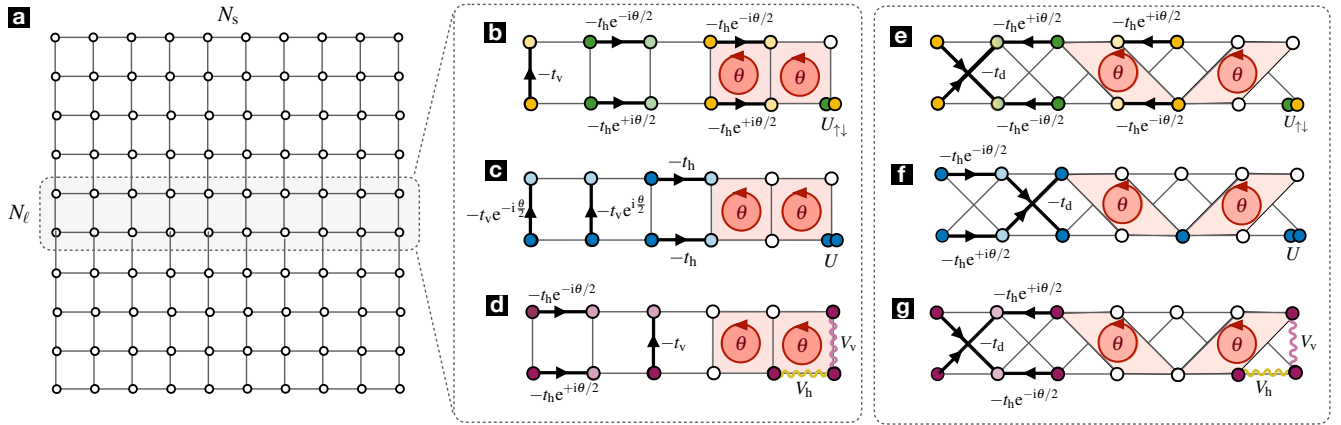


FIG. 1. **Hubbard ladders pierced by a magnetic field:** (a) Diagram of N_ℓ -leg ladder with open boundary conditions. Particles move across the ladder hopping along horizontal and vertical links that join the different lattice sites. (b) Rectangular 2-leg ladder for spin-full fermions subjected to an external magnetic flux θ . The fermions can hop along the legs and rungs with strength $t_h e^{\pm i\theta/2}$ and t_v , respectively, and interact through a repulsive local Hubbard interaction $U_{\uparrow\downarrow}$ depending on the spin. (c) Rectangular ladder for spin-less bosons subjected to an external homogeneous magnetic field. The tunneling strengths are arranged similarly to (b), and U represents the interaction strength when two bosons meet at the same lattice site. Exploiting the gauge freedom, one can arrange the Peierls' phases in the tunnelings along the vertical directions maintaining the same flux, such that the bosons pick an Aharonov-Bohm phase proportional to the flux θ when tunneling across a plaquette. (d) Rectangular ladder for spin-less fermions subjected to an external magnetic flux θ , here depicted though an anti-clockwise directed circle. The one-site Hubbard interaction is forbidden by Pauli exclusion, and only nearest-neighbor ones V_v and V_h can contribute. (e)-(g) Same as (b)-(d) but for a cross-linked, so called, Creutz-Hubbard ladder. Here, the tunneling between neighbouring chains occurs diagonally instead of vertically $t_v \rightarrow t_d$, forming a crossed-linked pattern. In this case, particles hopping along two possible trapezoidal plaquettes gain an Aharonov-Bohm phase proportional to the magnetic flux θ .

scope, as Lorentz invariance has also become manifest as an effective symmetry in systems of atomic, molecular and optical (AMO) physics [23, 24]. Building upon Feynman's idea of a quantum simulator [25], there has been a number of experiments targeting Lorentz- and gauge-invariant QFTs using ultracold atoms [26–31] and trapped ions [32–34] (see e.g. [35–39] for recent reviews). To the best of our knowledge, however, quantum simulations of Lorentz-violating extensions of the SM of particle physics have not been considered yet. Although Lorentz-breaking terms should in fact be the rule rather than the exception, since one starts from a non-relativistic model that accurately describes these AMO systems, the difficulty lies in tailoring those systems so that the Lorentz-violating terms that survive in the long-wavelength limit correspond precisely to those considered in the standard model extension (SME) [4]. This may change the role of the SME, which has routinely provided a framework for some of the most precise null experiments to date [40]. Instead, if successful, AMO quantum simulators have the potential to turn the SME into a framework of experimentally-testable analogue physics beyond the standard model. In this work, we follow this route for a particular case, unveiling interesting connections between Lorentz-violating quantum field theories and lattice models of correlated topological phases of matter that display a persistent chiral current. We show that the later provide a lattice regularisation of a specific matter sector of the SME including, in addition, four-Fermi Gross-Neveu-type interactions. Moreover, we also discuss how these models can

be implemented in experiments of ultra-cold atoms with synthetic spin-orbit coupling [41, 42].

This article is organised as follows: In Sec. II, we start by reviewing the physics of Hubbard ladders, which are the minimal fermionic lattice models that allow for the effect of external (background) gauge fluxes, and may support a circulating, so-called chiral, current. This sets the stage to introduce a particular lattice regularization of low-dimensional Lorentz-violating QFTs, the *cross-link Creutz-Hubbard ladder* for generic magnetic flux θ . We argue that this model can host a current-carrying topological crystalline phase, which is simultaneously described by a non-zero topological invariant and a circulating chiral current. A short summary of the main results of this work is then presented. In Sec. III, we explicitly construct the continuum limit of this ladder, and show that it corresponds to a *Gross-Neveu model extension* with a particular Lorentz violation that has been explored in the SME. This gives a neat perspective on the appearance of the persistent chiral current, which coexists with a non-zero topological invariant, and can be used to chart the phase diagram via the associated susceptibility, as discussed in Sec. IV. In Sec. V, using a self-consistent mean-field approach analogue to a large- N limit of the Gross-Neveu model, we study how this chiral current can be used to characterise the robustness of the topological crystalline phase as the strength of the four-Fermi interactions are increased, and discuss the full phase diagram of the model. We benchmark the mean-field predictions using tools developed by the condensed-matter and

quantum-information communities, i.e. tensor-network variational techniques based on matrix-product states. As discussed in the text, these quasi-exact numerics confirm qualitatively the mean-field prediction of the phase diagram, and correct the typical shortcomings of mean-field treatments. Finally, in Sec. VI, we present a proposal for a potential experimental realization with spin-orbit-coupled ultra-cold atoms. In this way, models of high-energy physics considered in the context of the Standard Model extension could be accessed with table-top experiments of non-relativistic neutral atoms at ultra-low temperatures.

II. THE CREUTZ-HUBBARD LADDER WITH ARBITRARY FLUX

In this section, we describe the model under study: the cross-linked Creutz-Hubbard ladder under an arbitrary magnetic flux. Let us start, however, by reviewing briefly the context of strongly-correlated behaviour in ladder compounds, which has a long and fruitful history in condensed matter.

A. Previous studies on Hubbard ladders

In ladder models, the particles are arranged on a lattice composed of N_ℓ chains with N_s sites each. Typically, these particles have nearest-neighbour couplings along the vertical and horizontal directions resembling a rectangular ladder structure of N_ℓ legs (see Fig. 1(a)). These systems interpolate between 1D and 2D as one increases the numbers of legs $N_\ell \rightarrow N_s$ and, sometimes, can host unexpected phenomena. For instance, in the context of Heisenberg ladders and their connection to the high- T_c cuprates [43], the parity of the number of legs determines the gapped/gapless nature of the model [44, 45], drawing a neat connection to the Haldane conjecture of spin chains and the interplay of topology and constrained QFTs [46, 47]. Through an analogue of the super-exchange mechanism [48], these Heisenberg ladders can be seen as the strong-coupling limit of a half-filled Hubbard ladder, where electrons interact via a strong local density-density coupling, the so-called Hubbard interaction [49]. Being quasi-1D, ladders yield a neat playground to generalise analytical methods [50–53] developed for one-dimensional systems [54]. Moreover, Hubbard and Heisenberg ladders can be explored numerically [55, 56] using efficient and very accurate numerical schemes [57, 58].

Getting closer to the subject of the present work, we note that the rectangular ladders are the minimal lattice structures that can be pierced by an external magnetic flux and have a well-defined thermodynamic limit (see Figs. 1(b)-(d)). By increasing the number of legs, these ladders yield a clear route towards the integer [59] and fractional [60] quantum Hall effects. For the two-leg ladder, the presence of a magnetic flux modifies the fermion tunnelling in a Hubbard ladder via the so-called Peierls' substitution [61] depicted in Fig. 1(b). This in turn leads to a rich phase diagram that contains Luttinger and Luther-Emery phases [62], depending on the magnetic

flux and the specific filling factor. In the case of spinless fermions, on-site Hubbard interactions must be exchanged for nearest-neighbour ones (see Fig. 1(d)), the interplay of which with the magnetic flux can also give rise to various strongly-correlated effects. While in the absence of the magnetic field, these finite-range interactions typically stabilise charge- and bond-density wave patterns depending on the particular filling, the situation becomes much richer as the magnetic field is switched on. For instance, one may find staggered flux phases with a pattern of local currents along the vertical and horizontal links, encompassing alternating circulations (i.e. vortices) in the plaquettes [63, 64]. Moreover, one can also find kinks/anti-kinks that interpolate between the two possible symmetry-broken patterns of vortices, each of which hosts fractionally-charged excitations in analogy to fractionalisation phenomena in QFTs [65] and polymers [66, 67].

The remarkable progress of ultra-cold atoms in optical lattices has stimulated a renewed interest in the physics of the bosonic counterparts of these ladders (see Fig. 1(c)). In particular, recent experiments [68, 69] have realised a Bose-Hubbard model [70, 71] in a two-leg ladder under an external magnetic flux. As discussed in previous theoretical works [72], this bosonic model can host liquid phases analogous to the Meissner and vortex phases of superconductors. These states of matter can be distinguished by a *circulating chiral current*, which has actually been measured in experiments [68]. This current quantifies a boson flow with a natural connection to the edge states and skipping orbits of quantum Hall samples as the numbers of legs is increased [73]. However, as the microscopic particles are bosons, the nature of the phases differs, and one can find novel Meissner- and vortex-type groundstates. In the Meissner phase, the bosonic chiral current plays the role of the screening current in superconductors (i.e. it flows in a different direction so as to screen the external magnetic flux). Alternatively, in the vortex phase, currents run along the ladder rungs leading to vortices where the magnetic flux is not fully screened, which draws a clear analogy to type-II superconductors. More recently, this distinction has also been identified as one increases the Hubbard interactions, where one finds Meissner- and vortex-type Mott insulators [74, 75], as well as the so-called vortex lattices [76, 77]. Let us also remark that the chiral current can also be used to unveil a quantitative connection of these quasi-1D ladders, both bosonic and fermionic, with the topologically-ordered phases [78] of the fractional quantum Hall effect [79, 80].

Once the relevant literature on fermionic and bosonic Hubbard models on rectangular ladders has been reviewed, let us describe the literature on *cross-linked Hubbard ladders*. In this case, the particles can tunnel between neighbouring chains forming a crossed-linked pattern, as depicted in Fig. 1(e)-(g). To the best of our knowledge, this ladder geometry was first introduced by M. Creutz [81, 82] in the context of domain-wall fermions [83–86] in lattice gauge theories [87, 88]. The presence of the external magnetic field changes considerably the band structure, and can even lead to completely flat bands in the π -flux regime [89], yielding an instance of Aharonov-Bohm cages [90] with fermions locked to the plaquettes due to destructive interference [81].

In fact, this so-called Creutz ladder is an archetype of flat-band physics [89]. In addition to these localised bulk states, there are additional edge states exponentially localised to the left- and right-most boundaries of the ladder. These states can be understood as lower-dimensional versions [81] of domain-wall fermions [83], and correspond to the edge states of a topological insulator [22] in the symmetry class AIII/BDI [91, 92]. The persistence of these topological features at finite temperatures [93, 94], and adiabatic [95] or sudden [96] dynamical quenches, has also been discussed in the literature. Moreover, the Creutz ladder also yields a neat scenario to explore the phenomenon of topological charge pumping [97].

Let us now briefly review some recent works exploring the strongly-correlated physics of this cross-linked ladder in the presence of Hubbard-type interactions. As occurred for the rectangular ladder, there has been a recent interest in studying the phases of a Bose-Hubbard model in this cross-linked geometry (see Fig. 1(f)). Here, a flat-band-induced frustration can change the standard condensation of bosons [98], and lead to new phases of matter even for weak interactions. Depending on the filling per site, the contact interactions can lead to valence bond crystals, quasi-superfluids of paired bosons, or supersolids that arise from bound pairs of domain walls that interpolate between two valence-bond orderings [99, 100]. We note that, in addition to the cold-atom quantum simulators, the bosonic Creutz-Hubbard ladder has also been discussed in the context of microwave photons in superconducting circuits [101], photonic waveguide arrays [102], and superradiant tight-binding lattices in momentum space [103]. Moving on to the spinful fermionic case of Fig. 1(e), this model yields a neat playground to understand correlation effects in topological phases of matter [104]. For instance, for attractive interactions and in the context of flat-band superconductivity [105, 106], one can find an exact Bardeen-Cooper-Schrieffer(BCS) groundstate and emerging $SU(2)$ symmetries [107]. In this case, a crossover between such BCS superconductor and a superfluid of tightly-bound pairs for attractive Hubbard interactions has also been found [108, 109]. The competition of BCS pairing and repulsive Hubbard interactions was discussed in [110], and shown to yield an interesting phase diagram with topological superconductors characterised by Majorana edge states. The interplay of flat-bands interactions and disorder has also been explored for the fermionic Creutz-Hubbard ladder [111, 112] in connection to many-body localisation [113].

The inclusion of various hyperfine states in cold-atom gases in optical lattices opens a new perspective for quantum simulations, as one may use the internal states as a synthetic dimension [114–116], as recently demonstrated in quantum simulators of quantum Hall ladders [117–119], or of spin-orbit coupled interacting wires [120–122]. In this context, the s -wave scattering that gives rise to $SU(N)$ Hubbard models [123, 124], can be understood as non-local interactions along the synthetic dimension of a rectangular ladder (see Fig. 1(b)-(d)), giving rise to a new family of models with a rich interplay between interaction-induced strong correlations and flux-induced kinetic frustration [80, 125–130]. As discussed in [131], the synthetic ladders are not restricted to rect-

angular geometries, as one can exploit Floquet-engineering techniques [132] to induce cross-link tunnelings, giving rise to the subject of this work: the *synthetic Creutz-Hubbard ladder*, which we now describe.

B. The synthetic Creutz-Hubbard ladder

We consider a system of spinless fermions that can be created (annihilated) at the sites of a two-leg ladder by the operators $c_{i,\ell}^\dagger$ ($c_{i,\ell}$), which are labelled by $i \in \{1, \dots, N_s\}$ and $\ell \in \{u, d\}$. The cross-link geometry of the ladder, as displayed in Fig. 1(g), is determined by the tunnelling terms of the lattice Hamiltonian

$$H_C = -\sum_{i,\ell} \left(t_h e^{-i\frac{s_\ell \theta}{2}} c_{i+1,\ell}^\dagger c_{i,\ell} + t_d c_{i+1,\ell}^\dagger c_{i,\bar{\ell}} - \frac{s_\ell \Delta \varepsilon}{2} c_{i,\ell}^\dagger c_{i,\ell} + \text{H.c.} \right), \quad (1)$$

where we have introduced the horizontal (diagonal) tunnelling strength t_h (t_d), the energy imbalance $\Delta \varepsilon$, and the notation $s_\ell = \{+1, -1\}$ and $\bar{\ell} = \{d, u\}$ for $\ell = \{u, d\}$, respectively. Finally, we note that the complex Peierls phases of the tunnellings lead to a non-zero Aharonov-Bohm phase θ when the fermions tunnel across the trapezoidal plaquettes depicted in Fig. 1(g). Accordingly, the parameter θ can be understood as the magnetic flux Φ_B of a background magnetic field $\mathbf{B}_{bg} = \nabla \times \mathbf{A}_{bg}$ that is directed perpendicularly to the plaquette S , $\theta = \frac{e}{\hbar} \oint_\gamma d\mathbf{l} \cdot \mathbf{A}_{bg} = 2\pi \frac{e}{\hbar} \int_S d\mathbf{S} \cdot \mathbf{B}_{bg} = 2\pi \Phi_B / \Phi_0$, expressed in units of the flux quantum $\Phi_0 = e/h$.

As advanced in the previous section, the $\theta = \pi$ -flux limit is obtained when half a flux quantum pierces each plaquette $\Phi_B = \Phi_0/2$, the tunnelings have equal strengths $t_h = t_d$, and the imbalance vanishes $\Delta \varepsilon = 0$. This leads to an Aharonov-Bohm destructive interference and a pair of flat bands $\varepsilon_\pm(k) = \pm 2t_h$, such that particle or hole excitations do not propagate $v_g = \partial_k \varepsilon_\pm(k) = 0$, where $k \in \text{BZ} = [-\pi/a, \pi/a]$ is the quasi-momentum of the reciprocal lattice for lattice spacing a . Moreover, these flat bands are topological, as they can be characterised by a non-zero topological invariant $\gamma_\pm = \mp \pi$ [131], the so-called Zak's phase $\gamma_\pm = \int_{\text{BZ}} dk \mathcal{A}_\pm(k)$ [133], where we have introduced the Berry connection $\mathcal{A}_\pm(k) = \langle \varepsilon_\pm(k) | i\partial_k | \varepsilon_\pm(k) \rangle$ [134]. As discussed in [131], the Berry connection in this π -flux limit is actually homogeneous $\mathcal{A}_\pm(k) = \mp 1/2$ which, in higher dimensions, would lead to a vanishing Berry curvature and one would speak of a topological flat-band structure. Let us also note that, by switching the energy imbalance $\Delta \varepsilon \neq 0$, the bands (connection) will no longer be flat (homogeneous), but the topological invariant remains quantised for $|\Delta \varepsilon| \leq 4t_h$. According to the underlying symmetries [135, 136], this imbalanced Creutz ladder hosts an AIII topological insulator.

The interplay of topology and interactions can lead to exotic phases of matter in topological flat-band systems [137]. In the context of synthetic dimensions in the cold-atom scheme [131], as discussed in more detail in Sec. VI, the upper and lower leg of the ladder actually correspond to two different hyperfine states of the groundstate manifold. Therefore, a contact Hubbard interaction due to the s -wave scattering of

the ultra-cold atoms can be interpreted as a nearest-neighbour interaction along the vertical direction connecting the legs of the synthetic ladder (see Fig. 1(g)). This leads to the following quartic term

$$H_{\text{CH}} = H_{\text{C}} + \frac{V_{\text{v}}}{2} \sum_{i,\ell} c_{i,\ell}^{\dagger} c_{i,\ell}^{\dagger} c_{i,\ell} c_{i,\ell}, \quad (2)$$

where $V_{\text{v}} > 0$ represents a repulsive interaction strength. As shown in [131] using various analytical and numerical techniques, the non-interacting AIII topological insulator is adiabatically connected to a *correlated topological insulator* in a wide lobe of parameter space $(V_{\text{v}}, \Delta\epsilon)$, the tip of which corresponds to $(V_{\text{v}}, \Delta\epsilon) = (8t_{\text{h}}, 0)$. This symmetry-protected topological phase is surrounded by a correlated trivial band insulator and an orbital ferromagnet. This symmetry-broken phase is characterised by the magnetic order parameter $M_{\text{y}} = \langle T_i^y \rangle \neq$

0, where $T_i^y = i(c_{i,\text{d}}^{\dagger} c_{i,\text{u}} - c_{i,\text{u}}^{\dagger} c_{i,\text{d}})/2$ can be understood as a spin-1/2 operator when the upper and lower leg components are interpreted as the two spin projections.

Interestingly, this π -flux regime has a direct connection to a Wilson-type discretization [138] of the Gross-Neveu (GN) model [139], a QFT of self-interacting fermions in (1+1) dimensions that shares some features with higher-dimensional non-Abelian gauge theories [88]. The GN model belongs to the family of four-Fermi field theories, originally introduced in the context of nuclear interactions by Enrico Fermi [140, 141]. Specifically, it can be understood as a low-dimensional version of Nambu-Jona-Lasinio (NJL) models [15, 16], and allows to explore chiral symmetry breaking by dynamical mass generation and asymptotic freedom in a renormalizable framework [139]. As discussed in [142, 143], the π -flux synthetic Creutz-Hubbard ladder can be unitarily mapped onto a Wilson-type discretization of the Gross-Neveu model, which is described by the following lattice Hamiltonian

$$H_{\text{GNW}} = a \sum_{x \in \Lambda_{\text{s}}} \left[\left(-\bar{\Psi}(x) \left(\frac{i\gamma^1}{2a} + \frac{1}{2a} \right) \Psi(x+a) + \bar{\Psi}(x) \left(\frac{m}{2} + \frac{1}{2a} \right) \Psi(x) + \text{H.c.} \right) - \frac{g^2}{2N} (\bar{\Psi}(x)\Psi(x))^2 \right], \quad (3)$$

where $\Psi(x) = (\psi_1(x), \dots, \psi_N(x))^{\text{t}}$ contains N flavours of the two-component Dirac spinors $\psi_n(x)$, $\bar{\Psi}(x) = \Psi(x)^{\dagger} \gamma^0$ is the adjoint, and γ^0, γ^1 are the gamma matrices in a (1+1)-dimensional spacetime $\{\gamma^{\mu}, \gamma^{\nu}\} = 2g^{\mu\nu}$, where $g^{\mu\nu} = \text{diag}(1, -1)$ is the flat Minkowski metric. For the synthetic Creutz-Hubbard ladder (1)-(2), one needs to set $N = 1$, $\psi_1(x) = \frac{1}{\sqrt{a}} \sin(\pi j/2) (c_{j,\text{u}}, c_{j,\text{d}})^{\text{t}}$ with $x = ja \in \Lambda_{\text{s}}$, and chose the gamma matrices $\gamma^0 = \sigma^z$, and $\gamma^1 = i\sigma^y$. The correspondence between the microscopic parameters is

$$\theta = \pi, \quad t_{\text{d}} = t_{\text{h}}, \quad ma = \frac{\Delta\epsilon}{4t_{\text{h}}} - 1, \quad \frac{g^2}{2N} = \frac{V_{\text{v}}}{4t_{\text{h}}}, \quad (4)$$

and the topological insulator lies in the BDI class. We note that digital quantum simulations of the GN model, including other discretizations such as the staggered-fermion approach, have also been discussed recently [144–146].

This connection yields interesting insights. On the one hand, it shows that the pseudo-scalar condensate $\Pi_0 = \langle \bar{\Psi}(x) i\gamma^5 \Psi(x) \rangle$, where $\gamma^5 = \gamma^0 \gamma^1 = \sigma^x$, corresponds exactly to the order parameter of the aforementioned orbital ferromagnet $\Pi_0 \leftrightarrow M_{\text{y}}$. This condensate acquires a non-zero value in the parity-breaking Aoki phase [147], and also plays a role in lattice discretization of quantum chromodynamics [148, 149]. Accordingly, the numerical results of [142] show that the existence of the Aoki phase, typically predicted in the basis of a large- N expansion [147], actually survives down to the ultimate quantum limit of $N = 1$. Moreover, from the perspective of the phase diagram of the Creutz-Hubbard ladder, this Aoki phase is not an artefact of the lattice scaffolding of the continuum fields, but rather a physical phase that delimits the correlated BDI topological insulator. On the other hand, the connection between these two models also shows that the stan-

dard continuum limit, where one recovers the continuum GN field theory [139], $a \rightarrow 0$ and $g^2 \rightarrow 0$, is actually the critical region separating the trivial and correlated topological insulators, and that it can be used to understand the strongly-coupled features of the topological phase diagram [143].

As can be seen in Eq. (4), however, the connection to the GN field theory and the interplay of topological phases and lattice discretizations (3) only apply to the π -flux regime of the synthetic Creutz-Hubbard ladder. It thus remains open to (i) explore the full phase diagram of the model (1)-(2) for arbitrary magnetic flux θ , (ii) find experimentally-accessible observables to characterise it, and (iii) unveil its connection to phenomena discussed in a high-energy context. In this work, we pursue this three-fold goal and find the results summarised in the following subsection.

C. Summary of the results

We have found that the Creutz-Hubbard ladder for arbitrary magnetic flux θ (1)-(2) has interesting connections between correlated topological phases of matter and Lorentz-violating QFTs in the SME. Interestingly, both the topological invariant that characterises these phases, and the coupling strength of the Lorentz-violating terms, can be controlled by modifying the value of the magnetic flux that pierces the ladder. As discussed in Sec. III, in the absence of interactions and for a particular set of bare microscopic couplings, the band structure of the model describes a semi-metal with a single Fermi point at momentum $k_{+} = \pi/2a$ or, otherwise, at $k_{-} = -\pi/2a$. The dispersion relation has a different propagation speed for right- and left-moving excitations, which clearly breaks

the emergent Lorentz invariance that appeared in the π -flux model [131]. Remarkably, we find that this Lorentz-breaking mechanism corresponds to a particular Lorentz violation of the SME, which also breaks parity and time-reversal symmetry [4]. In combination with Hubbard interactions, we show that the continuum limit is described by a Lorentz-violating GN model with four-Fermi terms that couple the Dirac spinors around each of these two Fermi points. We refer to this continuum limit as a Gross-Neveu model extension (GNME).

In Sec. IV, we discuss how the Lorentz violation in the GNME brings in a new feature. Whereas the π -flux Creutz-Hubbard ladder cannot support persistent currents in the groundstate, the breaking of Lorentz invariance due to the asymmetry in the speed of left- and right-moving particles can be responsible for a net current. In particular, in the non-interacting limit, we show that the groundstates can simultaneously display a non-zero topological invariant and a large chiral current circulating around the ladder, both of which are consistent with an inversion symmetry. Using the susceptibility associated to this chiral current, we chart the phase diagram of the model, and identify wide regions of parameter space with a current-carrying topological crystalline groundstate. In the limit of very strong Hubbard interactions, the half-filled ladder is described by an effective spin model that corresponds to the XY model with Dzyaloshinskii-Moriya super-exchange, and subjected to a transverse field. Depending on the value of the magnetic flux, one can either find ferromagnetic or anti-ferromagnetic phases, and second-order phase transitions that separate them from a disorder paramagnet that is preferred for sufficiently-large transverse fields.

In Sec. V, we show that the topological crystalline phases with a non-zero Zak's phase disappear in favour of these magnetic phases for sufficiently strong interactions. As a visual aid for the following discussions, we present a qualitative sketch of the phase diagram containing the various results in Fig. 2. In the parameter regime $\Delta\epsilon/4t_h \in (-1, 1)$ and $\theta \in (-\pi, \pi)$, we find that the Creutz-Hubbard ladder displays four distinct phases: a paramagnet (PM), a ferromagnet (FM_y), an anti-ferromagnet (AFM_x), and a topological crystalline phase (TCP). By using a mean-field reasoning in the effective GNME of the continuum limit, we understand how the effect of interactions contributes to various mass terms for the effective Dirac fermions, which provides a qualitative understanding of the fate of the topological phases when the four-Fermi interactions are increased. We make this discussion quantitative by finding the mean-field parameters self-consistently, and exploring the full phase diagram in detail. Although the specific critical lines are not accurate, we show that the structure of the phase diagram predicted by this self-consistent mean-field agrees with that obtained from a quasi-exact DMRG method. For weak interactions $V_v \ll t_h$, we show that the system has two topological lobes in parameter space $(V_v, \theta, \Delta\epsilon)$. This topological phase is protected by inversion symmetry, and can be thus identified with a correlated topological crystalline phase that is surrounded by a trivial band insulator, or by a symmetry broken phase with ferromagnetic (anti-ferromagnetic) long range order for large (small) fluxes $|\theta| \approx \pi$ ($\theta \approx 0$). Within these two lobes, the chiral current

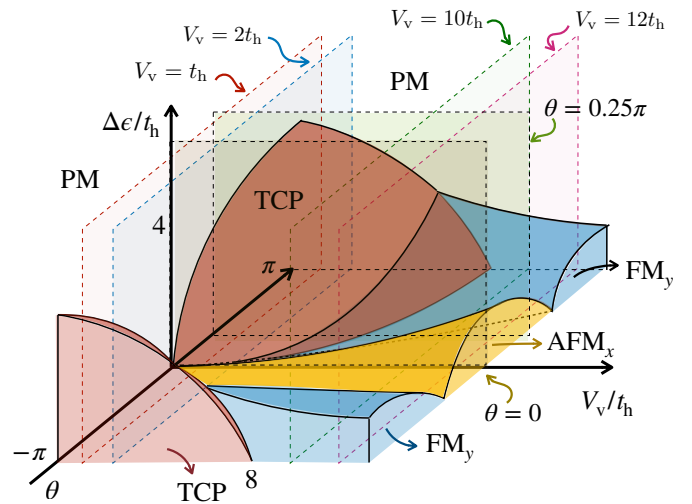


FIG. 2. **Schematic phase diagram for arbitrary fluxes:** Qualitative phase diagram of the Creutz-Hubbard ladder as a function of the Hubbard interactions V_v , the energy imbalance $\Delta\epsilon$, and the magnetic flux θ . At $|\theta| = \pi$, the topological phase in red is protected by a sublattice symmetry and belongs to the AIII class of topological insulators, which is surrounded by a topologically-trivial paramagnet (PM) in white, and a symmetry-breaking ferromagnet (FM_y) in blue, and delimited by second-order critical lines. For $|\theta| \lesssim \pi$, the sublattice symmetry is broken, and the topological phase is instead protected by inversion symmetry, representing a topological crystalline phase (TCP) which, in contrast to the π -flux limit, supports a large circulating chiral current. As the magnetic flux is decreased further towards $\theta \approx 0$, the TCP phase is also surrounded by a new symmetry-broken phase, an antiferromagnet (AFM_x) in yellow. We also depict shaded planes in parameter space where detailed numerical results are presented in the main text.

has a large absolute value and, despite the Lorentz-invariance breaking, the topological invariant remains to be non-zero $\gamma = \pm\pi$. The topological nature of this correlated phase is further confirmed by showing a 2-fold degeneracy of the entanglement spectrum, as calculated with our DMRG numerics. As one increases the interactions, the topological lobes become smaller, and there is a SSB process where the crystalline topological phase disappears in favour of the magnetic phases. Finally for $V_v \gg t_h$, we show that the DMRG results agree very well with those obtained from the effective spin model with anisotropic XY couplings and a Dzyaloshinskii-Moriya super-exchange.

An important aspect of the current work is that this interplay of topological phenomena, persistent chiral currents, and correlations in regularised Lorentz-violating QFTs can be realised in experiments of ultra-cold atoms in optical lattices. We show that modifying recent schemes of synthetic spin-orbit coupling using Raman optical lattices, one can realise the Creutz-Hubbard ladder with an arbitrary flux, being the latter tunable by adjusting the propagation direction and the frequency of the Raman beams. This scheme avoids the use of state-dependent optical lattices or Floquet-assisted tunnelings in interacting Fermi gases, minimising in this way the effective heating due to residual photon scattering from the

auxiliary excited states. In light of the recent experimental progress with Raman optical lattices [150–153], we believe that the current scheme opens a new direction in the realisation of strongly-coupled QFTs that incorporate Lorentz-violating terms of the SME, such as the GNME studied in this work. Additionally, the particular lattice regularization explored in this work would allow to explore the interplay of these relativistic models with current-carrying topological phases.

III. THE GROSS-NEVEU MODEL EXTENSION IN THE CONTINUUM LIMIT

We start by discussing the continuum limit of the Creutz-Hubbard ladder (1)-(2) for arbitrary flux $\theta \in (-\pi, \pi]$. In the rest of this work, we will set $t_d = t_h$ and consider half-filling conditions. One can diagonalise the non-interacting part (1) by a Fourier transform $c_{j,\ell} = \sum_{k \in \text{BZ}} e^{ikaj} c_{k,\ell} / \sqrt{N_s}$, which yields

$$H_C = \sum_{k \in \text{BZ}} \sum_{\ell, \ell'} c_{k,\ell}^\dagger h_{\ell\ell'}(k) c_{k,\ell'}, \quad h_{\ell\ell'}(k) = \varepsilon_0(k) \mathbb{I}_2 + \mathbf{d}(k) \cdot \boldsymbol{\sigma}, \quad (5)$$

where we have introduced the scalar and vector functions

$$\begin{aligned} \varepsilon_0(k) &= -2t_h \cos\left(\frac{\theta}{2}\right) \cos(ka), \\ \mathbf{d}(k) &= 2t_d \cos(ka) \mathbf{e}_x + \left(\frac{\Delta\varepsilon}{2} - 2t_h \sin\left(\frac{\theta}{2}\right) \sin(ka)\right) \mathbf{e}_z, \end{aligned} \quad (6)$$

and $\boldsymbol{\sigma} = \sigma^x \mathbf{e}_x + \sigma^y \mathbf{e}_y + \sigma^z \mathbf{e}_z$. Accordingly, the band structure is determined by diagonalizing the corresponding matrix, which yields the following two bands

$$\varepsilon_{\pm}(k) = \varepsilon_0(k) \pm |\mathbf{d}(k)|. \quad (7)$$

In the $\theta = \pi$ -flux regime, and setting $\Delta\varepsilon = 4t_h$ ($\Delta\varepsilon = -4t_h$), the band structure describes a semi-metal with a single Fermi point at $k_+ = +\pi/2a$ ($k_- = -\pi/2a$). As one modifies the flux $\theta \neq \pi$ and, simultaneously, adjusts the imbalance to $\Delta\varepsilon = \pm 4t_h \sin(\theta/2)$, the band structure still contains the single Fermi points at the same points of the Brillouin zone (see Figs. 3 (a) and (b)). Since the low-energy properties are controlled by particle/hole excitations around those Fermi points, the continuum limit is obtained by a long-wavelength approximation around them, where we define a spinor field

$$\psi(x) = \frac{1}{\sqrt{a}} (c_{j,u}, c_{j,d})^t \approx e^{ik_+ a} \Psi_+(x) + e^{-ik_- a} \Psi_-(x), \quad (8)$$

and separate the rapidly-oscillating parts $e^{ik_\eta a}$ from the slowly-varying operators $\Psi_\eta(x)$ for each of these Fermi points $\eta \in \{+, -\}$. These operators satisfy the desired anti-commutation relations in the continuum limit $a \rightarrow 0$, where $\{\Psi_{\eta,\ell}(x), \Psi_{\eta',\ell'}^\dagger(x')\} = \delta_{\eta,\eta'} \delta_{\ell,\ell'} \delta_{j,j'} / a \rightarrow \delta_{\eta,\eta'} \delta_{\ell,\ell'} \delta(x-x')$.

To obtain the QFT that governs this continuum limit, we use Eq. (8) and perform a gradient expansion for the fields $\Psi_\eta(x \pm a) = \Psi_\eta(x) \pm a \partial_x \Psi_\eta(x) + \mathcal{O}(a^2)$ to find the following

lowest-order expressions

$$\begin{aligned} \psi^\dagger(x) \hat{O}(\psi(x+a) + \psi(x-a)) &\approx 2ia \sum_{\eta} \eta \Psi_\eta^\dagger(x) \hat{O} \partial_x \Psi_\eta(x), \\ \psi^\dagger(x) \hat{O}(\psi(x+a) - \psi(x-a)) &\approx 2i \sum_{\eta} \eta \Psi_\eta^\dagger(x) \hat{O} \Psi_\eta(x), \end{aligned} \quad (9)$$

for any operator \hat{O} acting on the spinor degrees of freedom. Using these expressions, together with Eq. (8) and introducing the Hubbard interactions, we find that the continuum limit of the Creutz-Hubbard ladder (1)-(2) can be expressed as

$$\begin{aligned} H_{\text{CH}} &= \int dx \left(\sum_{\eta} \bar{\Psi}_\eta(x) (-i(c\gamma_\eta^1 + \tilde{c}_\eta \gamma_\eta^0) \partial_x + m_\eta c^2) \Psi_\eta(x) \right) \\ &\quad - \int dx \frac{g^2}{2} \left(\sum_{\eta} \bar{\Psi}_\eta(x) \Psi_\eta(x) + (-1)^{\frac{x}{a}} \bar{\Psi}_\eta(x) \Psi_\eta(x) \right)^2. \end{aligned} \quad (10)$$

The first line of this equation can be interpreted as the Hamiltonian QFT of a massive Dirac field for each of the species $\eta \in \{+, -\}$. These correspond to the so-called fermion doublers in the context of lattice gauge theories, which always yield an even number of species in the continuum limit [154, 155]. The corresponding gamma matrices are

$$\gamma_\pm^0 = \sigma^z, \quad \gamma_\pm^1 = \pm i \sigma^y, \quad \gamma_\pm^5 = \pm \sigma^x, \quad (11)$$

which shows that the continuum limit around each doubler carries an opposite chirality. The effective speed of light and mass of the Dirac fermions reads

$$c = 2t_h a, \quad m_\pm c^2 = \frac{\Delta\varepsilon}{2} \mp 2t_h \sin\left(\frac{\theta}{2}\right). \quad (12)$$

As customary in a Wilson-type discretization [138], the masses of the fermion doublers are no longer equal. This effect is not specific to the generic flux, as it also occurs in the π -flux model [131], where it underlies the existence of topological phases of matter. The result in Eq. (12) shows that one can achieve different Wilson masses for any flux $\theta \neq 0$, and that we can use the external flux to tune their relative values. In Fig. 3 (a), we see that when the flux is set such that $\Delta\varepsilon = -4t_h \sin(\theta/2)$, only the Dirac fermion at k_- remains massless, which agrees with the predictions in Eq. (12). On the other hand, for $\Delta\varepsilon = +4t_h \sin(\theta/2)$, it is the massless Dirac fermion at k_+ which controls the low-energy properties as depicted in Fig. 3 (b), which again agrees with Eq. (12). Note that, in order to use the natural units typical of relativistic quantum field theories, one must set $t_h = 1/2a$ above.

As one departs from the π -flux regime, a new term appears in the continuum limit (10) with the new coupling constant

$$\tilde{c}_\pm = \pm 2t_h a \cos\left(\frac{\theta}{2}\right). \quad (13)$$

This coupling introduces an explicit violation of Lorentz symmetry, which actually corresponds to a specific term in the

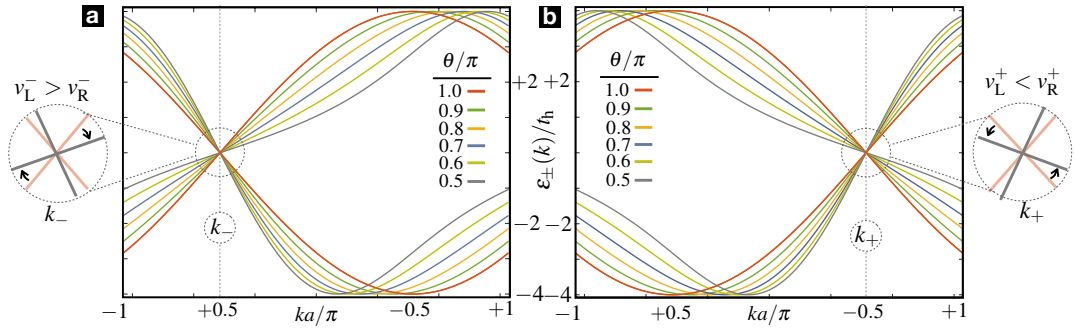


FIG. 3. **Band structure and Lorentz-violating Fermi points:** Dispersion relations $\varepsilon_{\pm}(k)$ (7) for the two bands of the imbalanced Creutz Ladder for different fluxes $\theta \in [\pi/2, \pi]$ (see the coloring labels of the insets). **(a)** The flux is set such that $\Delta\varepsilon = -4t_h \sin(\theta/2)$, and one can see that the low-energy properties are controlled by a massless Dirac fermion at $k_- = -\pi/2a$. **(b)** The flux is set such that $\Delta\varepsilon = 4t_h \sin(\theta/2)$, and one can see that the low-energy properties are controlled by the massless Dirac fermion at $k_+ = \pi/2a$. The left- and right-most insets show that the corresponding Dirac cones have different propagation speeds for right- and left-moving excitations, which read v_{R}^{\pm} and v_{L}^{\pm} .

standard model extension [4]. Before discussing the origin and consequences of this new term, let us comment on the second line of Eq. (10), which contains the coupling

$$\frac{g^2}{2} = \frac{V_v a}{2} = \frac{V_v}{4t_h}, \quad (14)$$

and is consistent with Eq. (4) in the single-flavour limit $N = 1$. We can see in Eq. (10) that this interaction term introduces, in addition to 4-Fermi terms for the separate species, mixing terms due to the back- and Umklapp-scattering that connect the two Fermi points of the original band structure. The appearance of these terms is standard in other 1D models at half-filling [54]. We note that these interaction-induced couplings between the two doublers play a key role in determining the renormalization-group flows of the microscopic parameters, which can be used to understand the shape of the phase diagram at $\theta = \pi$ [143]. We thus expect an analogous behaviour for generic fluxes, albeit leading to more complicated flow equations and a richer phase diagram.

Summarizing, we see that besides the new term (13), the continuum limit of the synthetic Creutz-Hubbard ladder for arbitrary flux corresponds to a fermion-doubled Gross-Neveu model, albeit with microscopic couplings that depend on the external flux θ . It turns out, however, that this additional term (13) changes the physics considerably, allowing us to explore some sectors of the SME. In order to unveil this connection, let us find the corresponding action $S_{\text{CH}} = \int d^2x (\sum_{\eta} \Pi_{\eta} \partial_0 \Psi_{\eta} - H_{\text{CH}})$, where the canonical momenta for each of the species are $\Pi_{\eta}(x) = ic\bar{\Psi}_{\eta}(x)\gamma_{\eta}^0$, and lead to

$$S_{\text{CH}} = \int d^2x \left(\sum_{\eta} \bar{\Psi}_{\eta}(x) (ic\Gamma_{\eta}^{\mu} \partial_{\mu} - m_{\eta} c^2) \Psi_{\eta}(x) \right) + \int d^2x \frac{g^2}{2} \left(\sum_{\eta} \bar{\Psi}_{\eta}(x) \Psi_{\eta}(x) + (-1)^{\frac{\eta}{a}} \bar{\Psi}_{\eta}(x) \Psi_{\bar{\eta}}(x) \right)^2, \quad (15)$$

where we use Einstein's summation convention for repeated spacetime indices $\mu, \nu, \tau \in \{0, 1\}$, and have introduced the

modified gamma matrices for each of the doublers

$$\Gamma_{\eta}^{\mu} = \gamma_{\eta}^{\mu} + c_{\eta}^{\mu\nu} g_{\mu\tau} \gamma_{\eta}^{\tau}. \quad (16)$$

In the context of the SME, $c^{\mu\nu}$ is a traceless tensor that contains the dominant corrections to the collisions of unpolarized electrons and positrons due to the violation of Lorentz invariance [6]. As discussed in the introduction, these terms may arise as an effective microscopic coupling from more fundamental theories at the Planck scale, such as string theory and non-commutative QFTs [2, 3]. It is remarkable that these terms arise naturally in the long-wavelength limit of the ladder. In the present context, we get one of these terms $c_{\eta}^{\mu\nu}$ for each doubler species $\eta \in \{+, -\}$ as a direct consequence of the $\theta \neq \pm\pi$ flux of the regularisation (1). In fact, we find that

$$c_{\pm}^{\mu\nu} = \begin{cases} \pm \cos(\frac{\theta}{2}) & \text{if } \mu = 1, \nu = 0 \\ 0 & \text{else,} \end{cases} \quad (17)$$

which becomes non-zero away from the π -flux regime, such that $\Gamma_{\eta}^0 = \gamma_{\eta}^0$, and $\Gamma_{\eta}^1 = \gamma_{\eta}^1 + \eta \cos(\frac{\theta}{2}) \gamma_{\eta}^0$. We note that, besides breaking Lorentz invariance, this term also breaks parity and time-reversal symmetry, although CPT is conserved [6]. As advanced previously, we refer to this continuum limit as a particular type of Gross-Neveu model extension.

A neat picture of the Lorentz violation caused by this term can be obtained by inspecting the band structure of Eq. (7) for generic fluxes, as depicted in Figs. 3(a) and (b). As already discussed in the previous section, when setting $\Delta\varepsilon = \pm 4t_h \sin(\theta/2)$, one obtains a semi-metal with a Fermi point at $k_{\pm} = \pm\pi/2a$. A closer inspection of the bands (see the left- and right-most insets of Figs. 3(a) and (b)) shows that the corresponding Dirac cone has a different propagation speed for right- and left-moving excitations, which reads as follows

$$v_{\text{R}}^{\pm} = 2t_h a \left(1 \pm \cos\left(\frac{\theta}{2}\right) \right), \quad v_{\text{L}}^{\pm} = 2t_h a \left(1 \mp \cos\left(\frac{\theta}{2}\right) \right). \quad (18)$$

This clearly breaks Lorentz invariance, as $\Delta\varepsilon = \pm 4t_h \sin(\theta/2)$ implies that the corresponding mass (12) vanishes, and the

fermion should thus be travelling at the same speed c (12) in both directions, regardless of the velocity of the frame of an inertial observer. However, for non-zero $c_{\eta}^{\mu\nu}$, inertial observers moving to the right or left will see the particle travelling at different speeds, such that Lorentz symmetry is broken.

This velocity difference suggests that there might be non-zero currents in the groundstate, as particles move faster in one direction than in the other. As show below, when the ladder has periodic boundary conditions, this flow of particles corresponds to a persistent chiral current that circulates in a specific direction set by the sign of the magnetic flux. For open boundary conditions, the persistent chiral current attains a fixed non-zero value at the bulk of the ladder, and gets attenuated as one approaches the left and right boundaries. Moreover, as also discussed below, this chiral current can be used to probe the full phase diagram.

IV. CHIRAL CURRENTS AND CRITICAL PHENOMENA

As discussed previously, the specific type of Lorentz violation that controls the low-energy properties (15) of the model predicts a different propagation speed for right and left-moving particles (18). In the underlying lattice discretization, this can yield a net *circulating chiral current* across the ladder

$$J_c = \sum_j \left(i t_h e^{i\frac{\theta}{2}} c_{j+1,u}^\dagger c_{j,u} - i t_h e^{-i\frac{\theta}{2}} c_{j+1,d}^\dagger c_{j,d} + \text{H.c.} \right). \quad (19)$$

This current measures the difference of the right- and leftwards fermion flows in the upper and lower legs of the ladder $J_c = J_u^\rightarrow - J_d^\leftarrow$, and thus gives rise to a sense of circulation/chirality (i.e. $\langle J_c \rangle > 0$ clockwise circulation, and $\langle J_c \rangle < 0$ anti-clockwise) that connects naturally with the current-carrying edge states of the quantum Hall effect as one increases the number of legs [73].

To avoid possible confusions, let us note that this circulating chiral current is not related to the axial current of continuum QFTs [1], which is also referred to as the chiral current, and is the Noether current associated to axial rotations. Note that for $N = 1$ [142], the four-Fermi term of the extended Gross-Neveu model (3) can be rewritten as

$$\frac{g^2}{2} (\bar{\Psi}(x)\Psi(x))^2 = \frac{g^2}{4} \left((\bar{\Psi}(x)\Psi(x))^2 - (\bar{\Psi}(x)\gamma^5\Psi(x))^2 \right), \quad (20)$$

such that the lattice model (3) including the Lorentz-violating term becomes invariant under continuous axial rotations $\Psi(x) \mapsto e^{i\alpha\gamma^5}\Psi(x)$, $\forall \alpha \in \mathbb{R}$. In the continuum limit, the Noether current associated to this symmetry is the aforementioned axial current $j_A^\mu = \bar{\Psi}(x)\gamma^5\gamma^\mu\Psi(x)$, which has a conserved axial charge given by

$$Q_A = \int dx j_A^0 = \int dx \bar{\Psi}(x)\gamma^5\Psi(x). \quad (21)$$

If we calculate the continuum limit of the circulating chiral current (19) using the fermion bilinear expressions of Eq. (9), we find that the leading-order contribution is

$$J_c = 2t_h \cos\left(\frac{\theta}{2}\right) \int dx \bar{\Psi}(x)\Psi(x) + \mathcal{O}(a), \quad (22)$$

which clearly differs from Q_A . We see that, away from the π -flux regime where the above expression (22) vanishes, the expectation value of the chiral current is proportional to the so-called scalar condensate $\Sigma_0 = \langle \bar{\Psi}(x)\Psi(x) \rangle$, the value of which marks the chiral symmetry breaking by dynamical mass generation of the standard Gross-Neveu model [139]. Therefore, this circulating current cannot be directly related to the axial current or to the chiral anomaly due to a background gauge field [156, 157]. In spite of this difference, given the transparent interpretation of two chiral windings, namely the anti-clock- and clock-wise circulations, it is customary to refer to this current as the chiral current.

In the following subsection, we shall characterise the phase diagram using this circulating chiral current and its associated susceptibility, which can be combined with the values of a topological invariant and a strongly-coupled effective theory to chart the full phase diagram of the model.

A. Chiral flows and topological phase transitions

Using the Hellmann-Feynman theorem, the expectation value of the chiral current can be expressed as the corresponding derivative of the total ground-state energy

$$\langle J_c \rangle = 2 \left\langle \frac{\partial H_{\text{CH}}}{\partial \theta} \right\rangle = 2 \frac{\partial E_{\text{gs}}}{\partial \theta}. \quad (23)$$

This quantity contains useful information about the phase diagram, which can already be seen at the non-interacting level. In this case, $E_{\text{gs}} = \frac{a}{2\pi} \int_{\text{BZ}} dk \varepsilon_-(k)$ is obtained by filling the N_s lowest energy states of Eq. (7), yielding

$$\langle J_c \rangle = -2t_h \cos\left(\frac{\theta}{2}\right) \int_{-\pi}^{\pi} \frac{dq}{2\pi} \frac{\frac{\Delta\varepsilon}{2} \sin q - 2t_h \sin(\frac{\theta}{2}) \sin^2 q}{|d(\frac{q}{a})|}, \quad (24)$$

where we have introduced $q = ka$. Additionally, we shall also be interested in the chiral susceptibility

$$\chi_c = \left\langle \frac{\partial J_c}{\partial \theta} \right\rangle = 2 \left\langle \frac{\partial^2 H_{\text{CH}}}{\partial \theta^2} \right\rangle = 2 \frac{\partial^2 E_{\text{gs}}}{\partial \theta^2} = \frac{\partial \langle J_c \rangle}{\partial \theta}, \quad (25)$$

which can be thus obtained by taking derivatives of the above integral (24) with respect to the flux.

In the main panel of Fig. 4, we represent the dependence of the chiral current with the magnetic flux for various positive values of the imbalance $\Delta\varepsilon > 0$. We observe the characteristic behaviour of a screening current, as also found in fermionic [64] and bosonic [72] rectangular ladders: the particles flow clockwise (counter-clockwise) $\langle J_c \rangle > 0$ ($\langle J_c \rangle < 0$) for positive (negative) flux $\theta > 0$ ($\theta < 0$) and, if charged, would thus induce a magnetic field that tends to screen the external one. In the bosonic case, this connects to the Meissner effect of a superfluid, while in the fermionic case it mimics the skipping orbits and edge states in quantum Hall samples (see the upper and lower insets of Fig. 4). This is consistent with the difference in the velocities of right- and left-moving particles v_R^+ , v_L^+ in Eq. (18), which control the low-energy dynamics in the vicinity of $\Delta\varepsilon = 4t_h \sin(\theta/2)$, which is the relevant case for the positive imbalances displayed in the Figure.

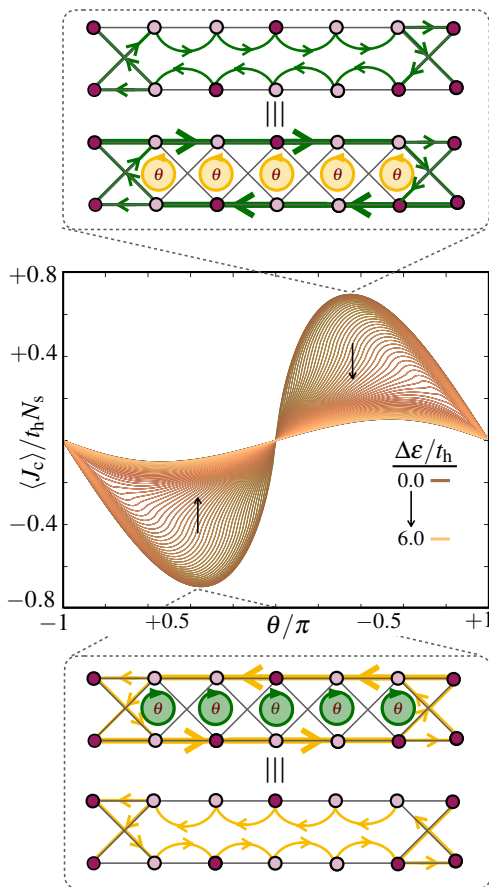


FIG. 4. **Chiral current in the synthetic Creutz ladder:** the main central panel presents the chiral current as a function of the magnetic flux for different imbalances $\Delta\epsilon$, using a coloring scheme that is specified in the index. In the upper and lower panels, we depict the particle flow clockwise (counter-clockwise) $\langle J_c \rangle > 0$ ($\langle J_c \rangle < 0$) for positive (negative) flux $\theta > 0$ ($\theta < 0$), and also draw the analog for the skipping orbits for fermions in a quantum Hall sample.

We also see in this figure that the chiral flow stops at the time-reversal symmetric points $\theta \in \{-\pi, 0, \pi\}$, which is again consistent with both right- and left-moving excitations traveling at the same speed. Note that for a vanishing flux $\theta = 0$, the band structure (7) for $\Delta\epsilon = 0$ contains a flat and a cosine-type band, such that one has to consider the two Fermi points with equal velocities $v_R^+ = v_L^-$ for the right- and left-moving excitations (see Fig. 5). The low-energy theory in this case is thus not given by Eq. (15) with Eq. (17) for $\theta = 0$, but rather by the standard Lorentz-invariant Luttinger liquid for a cosine band, which displays no circulating currents [54]. Accordingly, in both cases $\theta \in \{-\pi, 0, \pi\}$, there is no chiral current and we recover the effective Lorentz symmetry.

For the rectangular Hubbard ladders, the circulating chiral current has a different behavior. Its dependence with the flux displays a cusp-like behaviour that marks the onset of a Lifshitz transition where the number of Fermi points changes [62, 64]. Moreover, as one modifies the filling, the chiral current shows a linear dependence prior to the Lifshitz

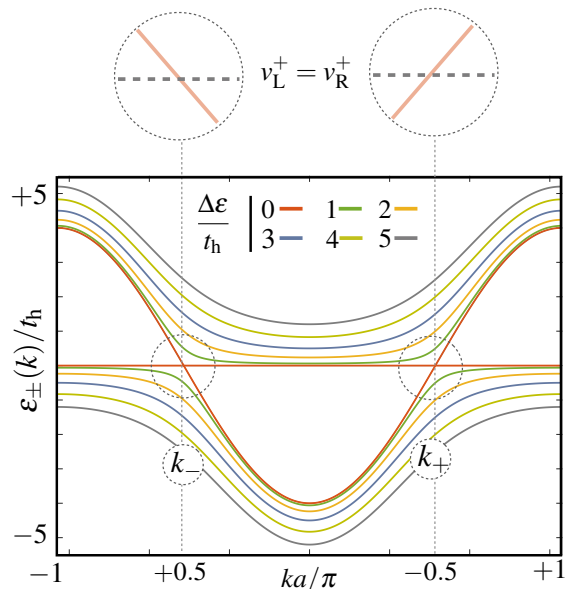


FIG. 5. **Bands for the Creutz ladder for vanishing flux:** Dispersion bands of the imbalanced Creutz ladder for $\theta = 0$ for different imbalance $\Delta\epsilon$, with a coloring specified in the inset. For $\theta = 0$ and $\Delta\epsilon = 0$ (red solid line) the band structure contains a flat and cosine-type band in which the two Fermi points have equal velocities $v_R^+ = v_L^-$ for right- and left-moving excitations.

transition that can be used to extract information about an underlying ladder-version of the Laughlin state in fractional quantum Hall phases [79, 80]. Although we do not find this exact phenomenology for the cross-linked ladder, the chiral current still carries information about phase transitions, albeit of a different nature. In order to see these effects, we now study the dependence of the chiral susceptibility with the magnetic flux. It turns out that the chiral susceptibility shows a clear divergence as $N_s \rightarrow \infty$ that coincides with the values of the imbalance $\Delta\epsilon = \pm 4t_h \sin(\theta/2)$, where the masses of the Dirac fermions (12) vanish. This divergence shall thus mark the onset of a gap closure, and a second-order phase transition instead of the aforementioned Lifshitz one.

In Figs. 6 (a) and (b), we show the contour plots of the chiral current and the chiral susceptibility, respectively, as a function of $(\theta/\pi, \Delta\epsilon/t_h)$. The chiral current shows much larger absolute values within the two lobes (see Fig. 6 (a)), and the maxima of the susceptibility serves to delimit the lobes and marks the phase transition (see Fig. 6 (a)).

To understand better the nature of this phase transition, we now discuss the values of the Zak phase [133] for arbitrary magnetic fluxes. This topological invariant, briefly discussed in the introduction, serves to characterise the topological phases of the Creutz ladder in the π -flux regime [131]. For generic fluxes, we find that the additional term $\epsilon_0(k)$ breaking particle-hole symmetry does not contribute to the Berry connection, such that

$$\gamma_{\pm} = \mp \int_{\text{BZ}} dk \frac{\mathbf{e}_y \cdot (\mathbf{d}(k) \times \partial_k \mathbf{d}(k))}{2|\mathbf{d}(k)|^2}, \quad (26)$$

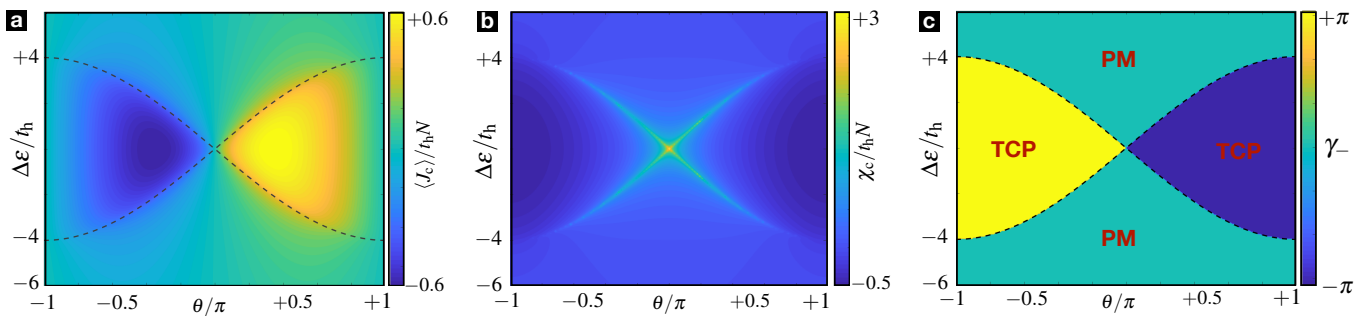


FIG. 6. **Phase diagram of the non-interacting Creutz ladder:** (a) The persistent circulating chiral current $\langle J_c \rangle$ in Eq. (24) is represented by a contour plot, and clearly displays a large non-zero value inside two lobes that touch at $\theta = 0$, surrounded by a region with a vanishingly-small particle flow. (b) Contour plot for the chiral susceptibility χ_c in Eq. (25), the maxima of which show a divergence with the number of sites N_s that delimits the lobes with a large non-zero chiral current, and marks the onset of a quantum phase transition. (c) Contour plot of Zak's phase in Eq. (27) as a function of the flux and imbalance. We see that the two lobes with a large chiral flow corresponds to the regions where the system is a topological crystalline phase with $\gamma_{\pm} = \pm\pi$, here represented by yellow/blue colors. The phase diagram thus consists of two regions with a topological-crystalline state that supports a large persistent chiral current except for $|\theta| \rightarrow \pi$, surrounded by a trivial band insulator with a vanishingly-small chiral current. The dashed black line of (a) shows the transition points from the topological to the trivial phases marked by the change of Zak's phase (28), which agree perfectly with the points where the chiral susceptibility diverges.

only depends on the Brillouin-zone vector field $\mathbf{d}(k)$ introduced in Eq. (6). We note that the contribution of the Berry connection to this topological invariant is actually concentrated around the two Fermi points $k_{\pm} = \pm\pi/2a$ around which we performed the long-wavelength approximation (10). This allows to calculate the integrals analytically, yielding

$$\gamma_{\pm} = \mp \frac{\pi}{2} \sum_{\eta=\pm} \eta \operatorname{sgn} \left(\frac{\Delta \epsilon}{2} - \eta 2t_h \sin \left(\frac{\theta}{2} \right) \right), \quad (27)$$

which is the difference of the signs of the two fermion masses in Eq. (12), $\gamma_{\pm} = \pm \frac{\pi}{2} (\operatorname{sgn}(m_-) - \operatorname{sgn}(m_+))$. This expression is analogous to the results found for higher-dimensional domain-wall fermions [85], and leads to the following critical lines that separate topological from trivial band insulators in the half-filled ladder

$$\gamma_- = \begin{cases} 0, & \text{if } \Delta \epsilon > 4t_h \left| \sin \left(\frac{\theta}{2} \right) \right|, \\ \pi, & \text{if } 0 < \Delta \epsilon < 4t_h \left| \sin \left(\frac{\theta}{2} \right) \right|, \\ -\pi, & \text{if } 0 > \Delta \epsilon > -4t_h \left| \sin \left(\frac{\theta}{2} \right) \right|, \\ 0, & \text{if } \Delta \epsilon < -4t_h \left| \sin \left(\frac{\theta}{2} \right) \right|. \end{cases} \quad (28)$$

Our results show that, in spite of our departure from the π -flux limit, and the associated breaking of Lorentz-invariance (16)-(17), one can still find a topological phase with a quantised non-zero Zak's phase in certain regions of parameter space.

This phase hosts edge states localised to the left/right boundaries of the ladder. In the π -flux limit [131], where the single-particle Hamiltonian (5) belongs to the AIII class $\{h(k), \sigma^y\} = 0$, the edge states are constrained to be zero-energy modes. In the present case, the underlying sub-lattice symmetry is broken, as $\{h(k), \sigma^y\} \neq 0$ for $\theta \neq \pi$. As a consequence, the topological phase is no longer within the AIII class, such that the edge states are no longer restricted to have zero energies. Even if no global symmetry is responsible for the protection of this topological phase, one can find a point-

like inversion symmetry

$$c_{i,u} \mapsto c_{N_s-i,d}, \quad c_{i,d} \mapsto c_{N_s-i,u}, \quad (29)$$

under which the Hamiltonian remains invariant $H_{\text{CH}} \mapsto H_{\text{CH}}$. Accordingly, groundstates with a quantized Zak phase can be understood as instances of a *topological crystalline phase* (TCP) [158–160]. Note that the above circulating chiral current (19) is also preserved under this ladder inversion $J_c \mapsto J_c$. The groundstate can thus display simultaneously a non-zero topological invariant protected by inversion symmetry, and a non-zero persistent circulating current, departing in this way from other topological crystalline insulators. Note that, in contrast to the two-dimensional quantum Hall effect, this circulating current is not carried by the edge states, which remain localised at the left/right boundaries. In Fig. 6 (c), we represent the contour plot of Zak's phase (27) as a function of $(\theta, \Delta \epsilon / t_h)$. By comparing to the contour plot of the chiral current in Fig. 6 (a), we see that the two lobes with a large circulating chiral flow correspond to regimes with non-zero $\gamma_{\pm} = \pm\pi$, in which the groundstate is a topological phase. As $\theta \rightarrow 0$, the topological insulator regions give way to a trivial band insulator with a vanishingly-small current. On the other hand, as $\theta \rightarrow \pm\pi$ towards the other time-reversal configurations, the circulating chiral current vanishes while the groundstate still supports a non-zero Zak's phase that ultimately yields the π -flux results of [131]. In the following sections, we explore how this picture gets modified as we include Hubbard interactions, starting from strong interactions.

B. Dzyaloshinskii-Moriya super-exchange

In this section, we discuss the nature of the phase diagram in the strong-coupling limit $V_v \gg t_h$ (i.e. $g^2 \gg 1$ in the language of the Gross-Neveu model (4)). As mentioned

in the introduction, in the strong-coupling regime, the half-filled rectangular Hubbard ladder for spin-full fermions can be described in terms of an effective anti-ferromagnetic Heisenberg ladder, where the origin of the spin-spin interactions can be understood as a super-exchange mechanism [48]. As shown in [131], the strong-coupling limit changes considerably for the cross-linked geometry in the π -flux limit. Here, one obtains ferromagnetic Ising interactions with a \mathbb{Z}_2 symmetry instead of the $SU(2)$ -invariant Heisenberg couplings. In the Ising case, one finds a symmetry-broken ferromagnet with magnetization $M_y \neq 0$ or, equivalently [142], a pseudoscalar condensate $\Pi_0 \neq 0$ in the language of the Gross-Neveu model. In both cases, there is a spontaneous symmetry breaking (SSB) process where the corresponding Altshuler-Lee-Pfeiffer topological insulator gives way to this long-range-ordered phase that breaks the \mathbb{Z}_2 symmetry. Since we have shown above that a current-carrying topological phase also appears for generic fluxes $\theta \neq 0$, it is interesting to explore if there is a similar SSB where it disappears in favour of a long-range order.

In the strong-coupling regime, due to the nature of the synthetic Hubbard interactions, the low-energy subspace will be spanned by fermion configurations that avoid double occupancies of two vertically-neighbouring sites of the ladder, as these doublons pay a large energy penalty. The leading-order dynamics comes from second-order processes $\mathcal{O}(t_h^2/V_v)$ where fermions tunnel back and forth virtually populating these doublons. At half-filling, all the possible second-order processes can be written in terms of orbital spin operators

$$\begin{aligned} T_i^x &= \frac{1}{2} \left(c_{i,u}^\dagger c_{i,d} + c_{i,d}^\dagger c_{i,u} \right), \\ T_i^y &= \frac{i}{2} \left(c_{i,d}^\dagger c_{i,u} - c_{i,u}^\dagger c_{i,d} \right), \\ T_i^z &= \frac{1}{2} \left(c_{i,u}^\dagger c_{i,u} - c_{i,d}^\dagger c_{i,d} \right). \end{aligned} \quad (30)$$

The second-order super-exchange processes lead to the following effective Hamiltonian of coupled orbital spins

$$\begin{aligned} H_{\text{DM}} &= \sum_i \left(J(1+\xi) T_i^x T_{i+1}^x + J(1-\xi) T_i^y T_{i+1}^y \right) \\ &+ \sum_i \left(\mathbf{D} \cdot (\mathbf{T}_i \times \mathbf{T}_{i+1}) + h T_i^z \right), \end{aligned} \quad (31)$$

where we have introduced the couplings

$$J = \frac{4t_h^2}{V_v} \cos \theta, \quad \xi = \sec \theta, \quad \mathbf{D} = -\frac{4t_h^2}{V_v} \sin \theta \mathbf{e}_z, \quad h = \Delta \varepsilon. \quad (32)$$

The first line of Eq. (31) represents the so-called XY model [161, 162] with spin-spin coupling strength J and anisotropy parameter ξ given in Eq. (32). The second-line of Eq. (31) contains a so-called *Dzyaloshinskii-Moriya interaction* [163, 164], which contains an anti-symmetric super-exchange with the coupling \mathbf{D} given in Eq. (32). Additionally, there is an external transverse field h also defined in Eq. (32).

Let us note that in the π -flux regime $\theta = \pi$, the Dzyaloshinskii-Moriya coupling and the xx interactions vanish $\mathbf{D} = \mathbf{0}$, $J(1+\xi) = 0$, while the yy interactions $J(1-\xi) =$

$-8t_h^2/V_v$ lead to the aforementioned Ising coupling, which favours a ferromagnetic long-range order along the y -axis, which coincides with the results of [131]. Conversely, for vanishing flux $\theta = 0$, it is $\mathbf{D} = \mathbf{0}$, $J(1-\xi) = 0$ which vanish, while the xx interactions $J(1+\xi) = +8t_h^2/V_v$ favour an anti-ferromagnetic long-range order. We thus expect that, as one varies the external magnetic flux, the direction and character of the long-range order within the xy plane will be modified.

Fortunately, the effective model turns out to be exactly solvable via Jordan-Wigner [165] and Bogoliubov [166] transformations. The first one allows us to express the orbital spin model in terms of a chain of spinless fermions, which in momentum space yields

$$H_{\text{DM}} = \sum_{k \in \text{HBZ}} \boldsymbol{\chi}_k^\dagger \left(\tilde{\varepsilon}_0(k) \mathbb{I}_2 + \tilde{\mathbf{d}}(k) \cdot \boldsymbol{\sigma} \right) \boldsymbol{\chi}_k. \quad (33)$$

Here, we have introduced the Nambu spinor $\boldsymbol{\chi}_k = (f_k^\dagger, f_{-k})^t$, which is expressed in terms of the new creation-annihilation operators of the Jordan-Wigner fermions within the halved Brillouin zone HBZ = $[0, \pi/a]$. The quadratic Hamiltonian in Eq. (33) depends on the scalar and vector functions

$$\begin{aligned} \tilde{\varepsilon}_0(k) &= \frac{4t_h^2}{V_v} \sin \theta \sin(ka), \\ \tilde{\mathbf{d}}(k) &= \frac{4t_h^2}{V_v} \sin(ka) \mathbf{e}_y + \left(\Delta \varepsilon - \frac{4t_h^2}{V_v} \cos \theta \cos(ka) \right) \mathbf{e}_z, \end{aligned} \quad (34)$$

which play an analogous role to those defined in Eq. (6) for the non-interacting limit of the Creutz-Hubbard ladder. Note, however, that the number of spinless Jordan-Wigner fermions is not conserved, as the transformed spin model is not invariant under $U(1)$ symmetry. Applying now a Bogoliubov transformation yields two energy bands analogous to Eq. (7)

$$\tilde{\varepsilon}_\pm(k) = \tilde{\varepsilon}_0(k) \pm |\tilde{\mathbf{d}}(k)|. \quad (35)$$

The groundstate energy in this case will be determined by filling all the momenta for which $\tilde{\varepsilon}_\pm(k) < 0$, which need not be N_s fermions as occurs for the original half-filled ladder with $U(1)$ symmetry. Therefore, the presence of a gap-closing phase transition can be predicted by finding the set of microscopic parameters that allow for $\tilde{\varepsilon}_\pm(k_0) = 0$, for some $k_0 \in \text{HBZ}$. One can only find a solution of this equation for a specific momentum $k_0 \in \{0, \pi/a\}$ if for $\Delta \varepsilon = \mp (4t_h^2/V_v) \cos \theta$. Accordingly, we identify two lines of second-order phase transitions at

$$\Delta \varepsilon_c(\theta) = \pm \frac{4t_h^2}{V_v} |\cos \theta|. \quad (36)$$

Let us now discuss the different phases that are delimited by these critical lines. In addition to the aforementioned SSB ferromagnetic and anti-ferromagnetic phases, the limit $h \gg |J|, |\mathbf{D}|$ can be easily understood. In this case, the orbital spins align in the opposite direction of the transverse field (31), which can be understood as an orbital paramagnet in which the original fermions are localised to the sites of the lower leg of the ladder. In Fig. 7, we present some

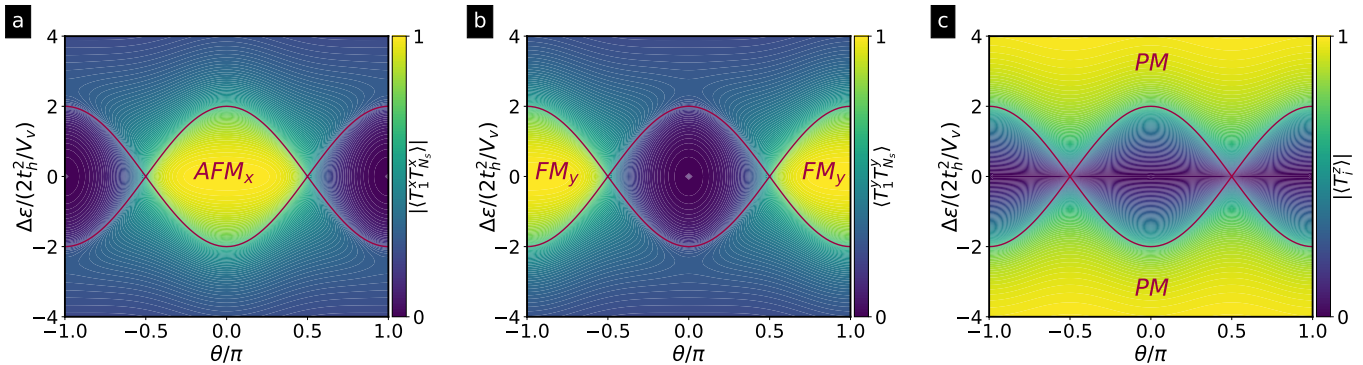


FIG. 7. **Phase diagram of the Creutz ladder for strong interactions:** Phase diagram displaying three different phases: ferromagnetic FM_y , anti-ferromagnetic AFM_x , and paramagnetic PM phases. The horizontal axis represent the flux per plaquette, whereas the vertical axis corresponds to the ratio of the energy imbalance to the super-exchange strength J . (a) The correlator $\langle T_1^x T_{N_s}^x \rangle$ is represented by a contour plot, quantitatively distinguishing a central yellow lobe where this correlator displays AFM_x long-range order. (b) We also represent the correlator $\langle T_1^y T_{N_s}^y \rangle$, which instead captures two lateral yellow lobes displaying FM_y long-range order. (c) The contour plot of the magnetization along the z direction $|\langle T_i^z \rangle|$ captures the paramagnetic phases, here represented by the yellow surrounding regions. The red lines correspond to the critical line in Eq. (36), and perfectly delimit the regions where the above observables characterise the various phases.

observables that allow to understand how these three different phases are arranged in this strong-coupling limit: (i) an anti-ferromagnet (AFM_x) aligned along the x axis occurs for $\Delta\epsilon < \Delta\epsilon_c(\theta)$ and $\theta \in (-\pi/2, \pi/2)$, (ii) a ferromagnet (FM_y) aligned along the y axis occurs for $\Delta\epsilon < \Delta\epsilon_c(\theta)$ and $\theta \in [-\pi, -\pi/2) \cup (\pi/2, \pi]$, and (iii) a paramagnet (PM) with all spins anti-aligned with the transverse field appears for $\Delta\epsilon > \Delta\epsilon_c(\theta)$ for any flux $\theta \in [-\pi, \pi]$ for sufficiently-large transverse fields. In Fig. 7 (a), we represent the two-point correlations functions $\langle T_1^x T_{N_s}^x \rangle$ in the groundstate of the orbital spin model, which tend to the AFM order parameter in the thermodynamic limit $|\langle T_1^x T_{N_s}^x \rangle| \rightarrow \langle T_1^x \rangle^2 = M_x^2$, which clearly displays a non-zero value in the inner yellow lobe. In Fig. 7 (b), we represent the two-point correlations functions $\langle T_1^y T_{N_s}^y \rangle$ in the groundstate of the orbital spin model, which tend to the FM order parameter in the thermodynamic limit $|\langle T_1^y T_{N_s}^y \rangle| \rightarrow \langle T_1^y \rangle^2 = M_y^2$, which clearly displays a non-zero value in two yellow lobes that touch the AFM_x phase at $\theta = \pm\pi/2$. Finally, in Fig. 7 (c), we represent the transverse magnetization $|\langle T_i^z \rangle|$, which becomes larger in the PM regions around the orbital magnets.

As noted at the end of the previous section, the topological crystalline phases supporting a persistent chiral current at zero interactions should disappear in favor of orbital magnetic phases as one increases the Hubbard interactions. The current strong-coupling analysis shows that these orbital magnets correspond to an AFM_x or FM_y depending on the magnetic flux. Additionally, the trivial band insulators that appear in the non-interacting limit should be adiabatically connected to the PM phases, as they both describe a limiting case in which all fermions occupy the sites of the lower leg for a very large energy imbalance. The question that will be addressed in the following section is how these two limiting cases are connected, and what is the nature of the quantum phase transitions that appear along the way, and how the chiral current/susceptibility can be used to characterised them.

V. PHASE DIAGRAM: SELF-CONSISTENT HARTREE-FOCK METHOD AND VARIATIONAL MATRIX-PRODUCT STATES

To address the question raised at the end of the previous section, and explore the full phase diagram of the model in the $\{\Delta\epsilon, \theta, V_v\}$ volume, we use two different methods: (i) a self-consistent mean-field approximation [167], and (ii) a variational method based on matrix-product states (MPS) [58].

As regards the first one, we start from the Hubbard interactions (2) and perform the Hartree-Fock decoupling

$$\frac{1}{2} \sum_{\ell} c_{i,\bar{\ell}}^{\dagger} c_{i,\ell}^{\dagger} c_{i,\ell} c_{i,\bar{\ell}} \approx \langle c_{i,u}^{\dagger} c_{i,u} \rangle c_{i,d}^{\dagger} c_{i,d} + \langle c_{i,d}^{\dagger} c_{i,d} \rangle c_{i,u}^{\dagger} c_{i,u} - \langle c_{i,u}^{\dagger} c_{i,d} \rangle c_{i,d}^{\dagger} c_{i,u} - \langle c_{i,d}^{\dagger} c_{i,u} \rangle c_{i,u}^{\dagger} c_{i,d}, \quad (37)$$

where we have neglected a c -number that will contribute equally to the energies of all possible eigenstates of the mean-field Hamiltonian. After this Hartree-Fock decoupling, the Hamiltonian (1)-(2) is expressed as the sum of quadratic terms

$$H_{\text{CH}}^{\text{mf}} = \sum_{i,\ell} \left(t_h e^{-i\frac{s\theta}{2}} c_{i+1,\ell}^{\dagger} c_{i,\ell} + t_d c_{i+1,\ell}^{\dagger} c_{i,\bar{\ell}} - \frac{s_{\ell} \Delta\epsilon}{2} c_{i,\ell}^{\dagger} c_{i,\ell} + \frac{1}{2} \epsilon_{\ell} (\{n_{i,\bar{\ell}}\}) c_{i,\ell}^{\dagger} c_{i,\ell} + t_{\ell} (\{b_{i,\bar{\ell}}\}) c_{i,\ell}^{\dagger} c_{i,\bar{\ell}} + \text{H.c.} \right). \quad (38)$$

Here, we have introduced a shift of the on-site energies ϵ_{ℓ} that depends on the local fermion numbers $n_{i,\bar{\ell}} = \langle c_{i,\bar{\ell}}^{\dagger} c_{i,\bar{\ell}} \rangle$, together with a vertical tunneling term t_{ℓ} that depends on the bond densities $b_{i,\bar{\ell}} = \langle c_{i,\bar{\ell}}^{\dagger} c_{i,\ell} \rangle$. The former, which is always a real number, will play an important role when the fermions distribute differently along the two legs of the ladder; whereas the later, which can be a complex number, shall determine how the fermions delocalise over the vertical links of the ladder. These parameters are both proportional to the Hubbard

interaction

$$\varepsilon_\ell(\{n_{i,\bar{\ell}}\}) = V_v \langle c_{i,\bar{\ell}}^\dagger c_{i,\bar{\ell}} \rangle, \quad t_\ell(\{b_{i,\bar{\ell}}\}) = V_v \langle c_{i,\bar{\ell}}^\dagger c_{i,\ell} \rangle. \quad (39)$$

The on-site energy shifts will renormalise the energy imbalance, changing in accordance the extent of the non-interacting phases. In addition, the vertical tunnelings can change the physics considerably, as they modify the effective connectivity of the ladder. In the non-interacting case, inter-leg tunnelings can only occur via cross-link hoppings whereas, in the presence of interactions, these mean-field terms can allow for such hoppings occurring vertically.

We note that the mean-field approximation requires the observables $\{n_{i,\ell}, b_{i,\ell}\}_{i=1}^N$ to be determined self-consistently, and we must deal with a number of self-consistency equations that grows linearly with the number of sites. The self-consistent loop consists in the following steps: (i) we start by setting an initial configuration of densities $\{n_{i,\ell}\}$ and bond densities $\{b_{i,\ell}\}$ for different phases. As regards the AFM_x ordering, we have chosen a pattern of real numbers with alternating signs for bond densities $\{b_{i,\ell}\}$ and alternation of 0 and 1 for $\{n_{i,\ell}\}$ such that $\sum_i (n_{i,u} + n_{i,d}) = N_s$. Instead, when the target is the topological crystalline phase or the FM_y, it is better to start from a translationally-invariant pattern of complex numbers for $\{b_{i,\ell}\}$. Moreover, for the PM phase, we start from a translationally-invariant pattern of real numbers for $\{b_{i,\ell}\}$ and we fixed $n_{i,u} = 1$ and $n_{i,d} = 0 \forall i$. (ii) Given these initial seeds, we diagonalise the fermionic tight-binding model defined in Eq. (38), and get another estimate of the mean-field parameters (39). We then iterate this process until the self-consistent parameters and the energy converge with an error of 10^{-8} .

Let us now discuss these different mean-field configurations at the level of the continuum QFT (9). Assuming a translationally-invariant half-filled groundstate, one finds that an occupation imbalance on the legs $\Delta n_i = n_{i,u} - n_{i,d} = \Delta n, \forall i$ shifts the Wilson masses in Eq. (12) as follows

$$m_\pm c^2 \mapsto \tilde{m}_\pm c^2 = \frac{\Delta\varepsilon - V_v \Delta n}{2} \mp 2t_h \sin\left(\frac{\theta}{2}\right), \quad (40)$$

This can readily be interpreted as the aforementioned renormalisation of the energy imbalance $\Delta\varepsilon \rightarrow \Delta\tilde{\varepsilon}$. A positive bare energy imbalance $\Delta\varepsilon > 0$ favors the occupation of fermions on the lower leg $\Delta n < 0$, which in turn increases the renormalised energy imbalance $\Delta\tilde{\varepsilon} = \Delta\varepsilon + V_v |\Delta n|$ in Eq. (40). Consequently, the critical lines where one of the Wilson masses (28) gets inverted will be shift towards smaller values of the bare energy imbalance $\Delta\varepsilon$ when the Hubbard interactions are increased, such that the self-consistent topological regions shrink in favor of the mean-field trivial band insulator.

Motivated by the strong-coupling results of the previous section, another possibility for a translationally-invariant groundstate is that of a purely imaginary bond density $b_{i,u} = \langle c_{i,u}^\dagger c_{i,d} \rangle = -b_{i,d} = iM_y, \forall i$. Such arrangement of bond densities corresponds to the orbital ferromagnet FM_y found in the previous section for sufficiently strong couplings and fluxes. This type of order is induced by the mean-field vertical tunnelings (39) and, in the continuum QFT (9), leads to a new

kind of mass term

$$m_\eta c^2 \bar{\Psi}_\eta \Psi_\eta \rightarrow \tilde{m}_\eta c^2 \bar{\Psi}_\eta \Psi_\eta + \eta V_v M_y \bar{\Psi}_\eta \gamma_\eta^5 \Psi_\eta. \quad (41)$$

These two self-consistent masses are renormalised by the imbalance and bond densities, which correspond to the aforementioned scalar and pseudo-scalar condensates of the Gross-Neveu model with a Wilsonian regularization [142]. If the interactions are strong enough, the ferromagnet will be formed $M_y \neq 0$, such that the Zak's phase will no longer be quantised (28) as a consequence of the two non-zero masses. Moreover, the long-range order is incompatible with the protecting symmetries, and the ferromagnet fully expels the topological crystalline phase via a SSB phase transition.

Again motivated by the strong-coupling results, we should consider a bond-density wave that breaks translation invariance. This is given by a purely-real alternating bond density $b_{i,u} = \langle c_{i,u}^\dagger c_{i,d} \rangle = b_{i,d} = (-1)^i M_x, \forall i$, corresponding to the orbital anti-ferromagnet AFM_x, which was found for sufficiently strong couplings and small magnetic fluxes (see Fig. 7). In light of this order parameter, we see that in the limit $M_x \rightarrow 1$, fermions delocalise along the vertical rungs of the ladder with an alternating symmetric/anti-symmetric pattern. Such an alternating pattern leads to a different long-wavelength term, as it effectively couples the two species of Dirac fermions by the following Umklapp term

$$m_\eta c^2 \bar{\Psi}_\eta \Psi_\eta \rightarrow \tilde{m}_\eta c^2 \bar{\Psi}_\eta \Psi_\eta - V_v M_x \bar{\Psi}_\eta \Psi_{\bar{\eta}}. \quad (42)$$

At zero magnetic flux, where the band structure in Fig. 5 displays a flat band and a cosine band, one may form a massless Dirac spinor from the right- and left-moving components at $k_\pm = \pm\pi/2a$, such that the gap-opening Umklapp term corresponds to yet a different mass term. Although, at the mean-field level [13], the massless Dirac fermion is unstable towards the alternating bond-density wave for arbitrary-small interactions, the presence of the flat band and the correlations beyond mean-field may change this simple picture. In any case, if this bond-density wave is formed, the topological invariant will no longer be quantised (28), and the associated anti-ferromagnet will fully expel the topological phase.

Let us note that this self-consistent mean-field method is equivalent to a large- N limit of the equivalent Gross-Neveu model, where one introduces auxiliary bosonic fields via a Hubbard-Stratonovich transformation [168], and sends the number of fermionic species $N \rightarrow \infty$. In the π -flux limit, it suffices to introduce a couple of auxiliary fields, the non-zero expectation values of which lead to the onset of the so-called scalar and pseudo-scalar condensates discussed in Sec. II B. We have checked that our self-consistent mean-field approach provides numerical results that are in complete agreement with the large- N prediction of the π -flux limit presented in [142]. As one modifies the magnetic flux, the large- N approach should be generalised to include an additional auxiliary field, the condensation of which would be connected to the AFM_x order. Instead of following this approach, which requires solving a new set of coupled non-linear gap equations, the current self-consistent mean-field is sufficiently general so that it can directly encompass any type of ordering, and

such an order can be efficiently found by a suitable choice of the initial seed.

In any case, both the mean-field and the large- N methods do not take the inter-particle correlations in full account. For this reason, we benchmark these results with matrix-product state (MPS) methods. In particular, we use the density matrix renormalization group (DMRG) based on MPS, which is becoming a very useful tool to explore lattice discretizations of quantum field theories [36, 169]. This can be considered as the most stringent test of the validity of the mean-field approach. We consider lattices up to $L = 128$ sites and virtual dimension up to $\chi = 200$. Our DMRG code is based on MPS and uses a two-site optimization scheme. It is built implementing the Abelian symmetries such as a particle conservation. Indeed, we fix half-filling and open boundary conditions.

A. Weak and intermediate interactions

In this section, we analyze the effect of correlations in the phase diagram of the Creutz-Hubbard ladder under a generic magnetic flux, focusing on the regime of weak interactions.

We start by setting $V_v/t_h = 1.0$ and $V_v/t_h = 2.0$, which correspond to the red and green shaded planes of the schematic phase diagram of Fig. 2. Our numerical results for the phases of matter that appear in these planes are presented in Fig. 8, where we have used self-consistent mean-field and DMRG methods. The lines represent the critical points where the topological and SSB phase transitions occur, either obtained with a DMRG method based on finite MPS with bond dimension $\chi = 200$ (red stars), or by the self-consistent Hartree-Fock method (yellow dashed lines). As can be observed in the figure, for weak interactions, the Hartree-Fock and DMRG critical points separating the TCP and PM regions yield two critical lines that are very similar to each other. The main differences appear in the critical lines separating the AFM_x and PM phases, as the mean-field method predicts a smaller AFM_x . Let us now analyze this figure in more detail, and describe the methodology used to extract these critical points.

In analogy with the non-interacting case (1), the ground-state of the weakly-interacting Creutz-Hubbard ladder (2) contains a topological crystalline phase (TCP) as one departs from the π -flux limit. As discussed qualitatively around Eq. (40), one of the expected effects of interactions is to shrink the size of the TCP lobes in favor of the trivial band insulator. Note that the trivial band insulator is adiabatically connected to the orbital PM when the energy imbalance is increased, and we refer to them interchangeably. This shrinking can be readily observed by comparing the vertical extent of the TCP lobes in the non-interacting and interacting cases (compare Figs. 6 and 8). Moreover, as shown in Sec. VC, the entanglement spectrum on these lobes is two-fold degenerate (see Fig. 15 a hallmark of symmetry-protected topological phases [170]). This shows that the non-interacting TCPs discussed in Sec. IV A is adiabatically connected to these correlated TCP lobes. Comparing Figs. 8 (a) to (b), we also see that the shrinking of the TCP in favor of the PM increases with the strength of the Hubbard interactions, which is a di-

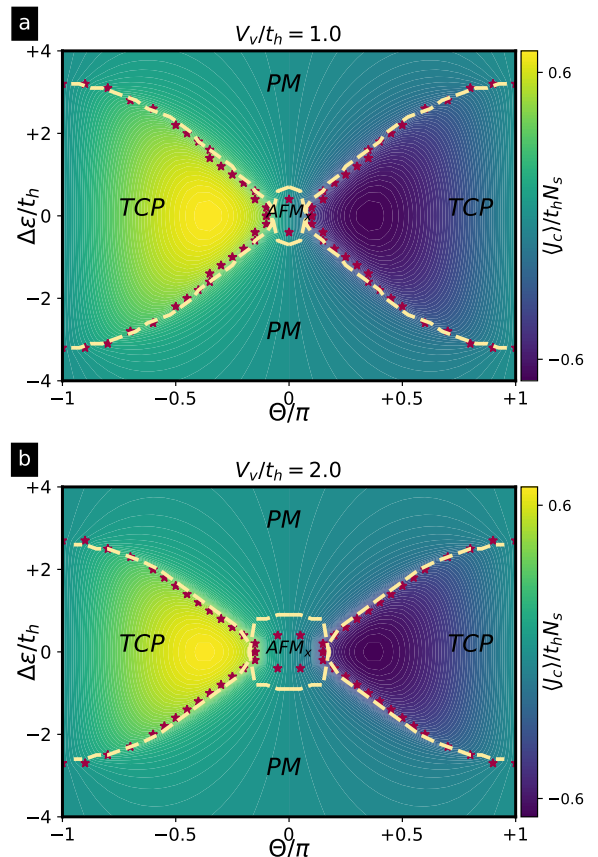


FIG. 8. **Phase diagrams for weak interactions:** (a) $V_v/t_h = 1$, (b) $V_v/t_h = 2$: The phase diagrams display two regions hosting a topological crystalline phase (TCP), a long-range-ordered anti-ferromagnetic phase (AFM_x), and a paramagnetic phase (PM). The horizontal axis represents the magnetic flux, whereas the vertical axis corresponds to the ratio of the energy imbalance to the tunneling strength. The red stars (yellow dashed lines) show the critical points found from DMRG (self-consistently mean-field) numerics. These points are plotted on top of the contour plot of the chiral current, obtained by calculating Eq. (19) using DMRG.

rect consequence of the interaction-induced renormalization of the Dirac-fermion masses (40) in the continuum QFT.

Let us also recall that, as argued in Sec. III, the violation of Lorenz symmetry in the continuum QFT (15)-(16) can be associated to a different propagation speed for right- and left-moving particles (see the insets of Fig. 3). This difference can give rise to a net circulating chiral current, serve to characterise further the phases of the model, and may act as a good indicator to predict the critical lines (see Fig. 6 (a)-(b)). In particular, we recall that the non-interacting TCP supports large values of this permanent chiral current away from the π -flux limit (see Fig. 6 (a)). In the background of Figs. 8 (a) and (b), we present the expectation value of the chiral current $\langle J_c \rangle$ in Eq. (19) in the presence of interactions, as obtained by the DMRG numerics. We see that, as the TCP lobes shrink in size due to the Hubbard interactions, the area with a large chiral current also decreases. Therefore, the correlated TCPs can still support large chiral currents around the ladder.

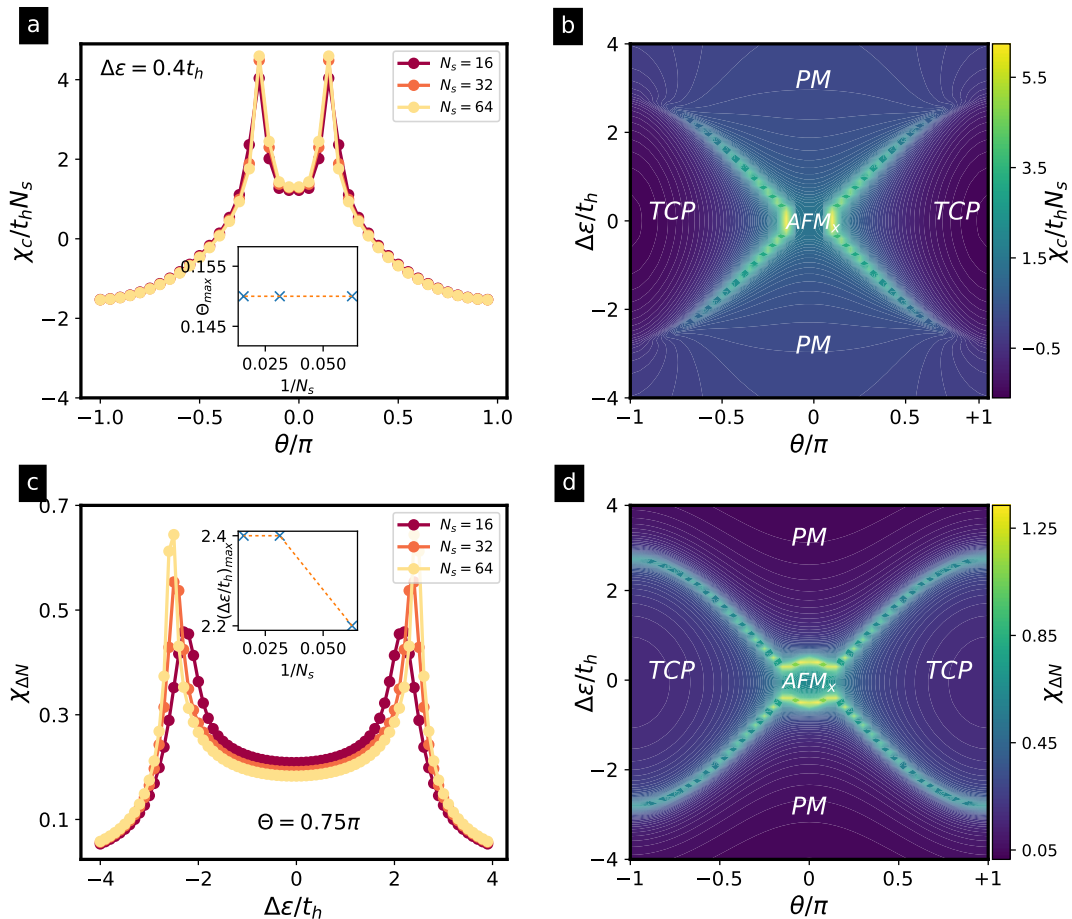


FIG. 9. **Chiral and imbalance susceptibilities:** (a) The peaks of the chiral susceptibility χ_c with growing system size $N_s \in \{16, 32, 64\}$ allow to locate the critical point for a cut of phase diagram at $V_v = 2t_h$ and $\Delta\varepsilon = 0.4t_h$. (b) The contour plot of the chiral susceptibility for system size $N_s = 64$, delimiting the TCP lobes from other phases. (c) The peaks of the imbalance susceptibility $\chi_{\Delta n}$ with growing system size $N_s \in \{16, 32, 64\}$ allow to locate the critical points also around the π -flux regime. (d) The contour plot of the imbalance susceptibility for system size $N_s = 64$.

The critical points delimiting the TCP lobes in the phase diagram are estimated via the chiral susceptibility $\chi_c = \partial \langle J_c \rangle / \partial \theta$ (25). We recall that, in the non-interacting limit, this susceptibility presents a divergence at the critical points (see Fig. 6 (b)). In Fig. 9 (a), we display the chiral susceptibility for ladders with a different number of sites per leg $N_s \in \{16, 32, 64\}$, fixing the energy imbalance $\Delta\varepsilon = 0.4t_h$ and interaction strength $V_v = 2t_h$, and varying the external magnetic flux. These numerical results clearly show a peak at two symmetric values of the magnetic flux with respect to the zero-flux axis. The finite size scaling (FSS) of the chiral susceptibility maxima as a function of N is displayed in the inset. As one can see in the inset, the peak of the chiral susceptibility diverges with the size of the ladder, and fitting the maxima of θ_c to $\theta_c(N) = \theta_c(1 + aN^{-1} + bN^{-2})$, we can delimit the TCP lobes and locate the phase transitions. In Fig. 9 (b), we show the contour plot of the chiral susceptibility with the corresponding peaks, which clearly shows how the critical lines separate the TCP from other phases. Comparing to the non-interacting case in Fig. 6 (b), we clearly see that these critical

points are moved towards smaller imbalances, which underlies the shrinking of the TCP lobes.

So far, our numerical benchmark has focused on the TCP phase, and revolved around quantities related to the circulating chiral current. An alternative way of identifying this phase boundary is by studying the occupation leg imbalance

$$\Delta n = \frac{1}{N_s} \sum_j \left(\langle c_{j,u}^\dagger c_{j,u} \rangle - \langle c_{j,d}^\dagger c_{j,d} \rangle \right). \quad (43)$$

The occupation imbalance is induced by a non-zero energy imbalance $\Delta\varepsilon$, which motivates the definition of an imbalance susceptibility $\chi_{\Delta n} = \partial \Delta n / \partial \Delta\varepsilon$ that proved to be a good indicator of the quantum phase transition in the π -flux limit [131], and can be easily calculated using our DMRG code. In Fig. 9 (c), we show the imbalance susceptibility for ladders with a different number of sites per leg $N_s \in \{16, 32, 64\}$, fixing the magnetic flux to $\theta = 3\pi/4$, the Hubbard interactions to $V_v = 2t_h$, and varying the energy imbalance $\Delta\varepsilon$. Once again, this susceptibility shows a pair of peaks that are symmetric with respect to the zero-imbalance axis. A FSS shows that

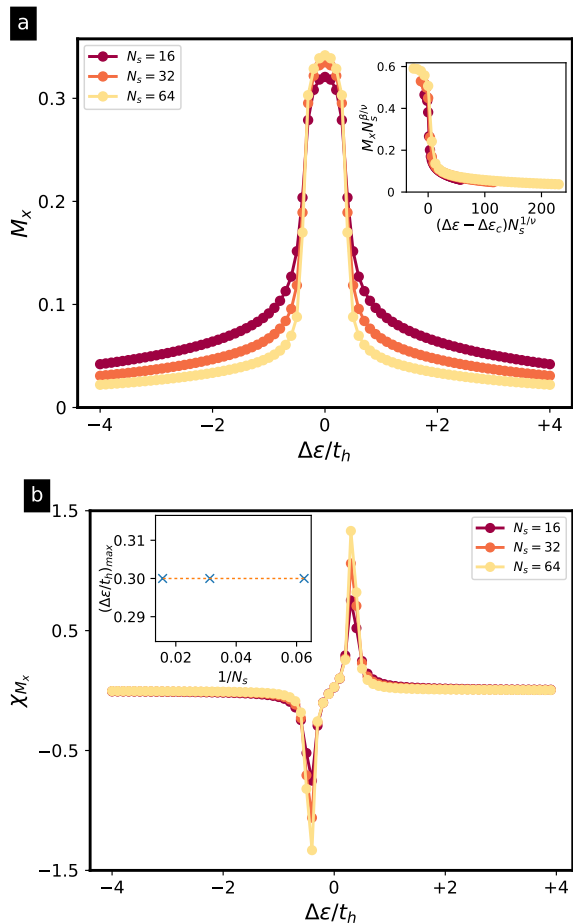


FIG. 10. **Staggered magnetization and magnetic susceptibility:** (a) Staggered magnetization for fixed interaction strength $V_v = 2t_h$ and flux $\theta = \pi/10$, and different number of sites per length $N_s \in \{16, 32, 64\}$. As the length increases, the systems develops a non-zero expectation value only within a symmetric region around zero imbalance. (b) The magnetic susceptibility χ_{M_x} for the same parameters shows a couple of peaks that increase with the system size, and allow us to locate the critical points.

this peak actually diverges in the thermodynamic limit, and allows us to locate the position of the critical point. The critical points obtained through this analysis are represented in a contour plot in Fig. 9 (d). As can be seen from these results, this susceptibility is more effective than the chiral one in the critical regions around π -flux, which is to be expected since the chiral current vanishes in these regions.

The main difference brought up by the interactions occurs in the region of small magnetic fluxes, where the Umklapp term (42) may dominate over the other gap-opening mechanisms. This term is expected to stabilize a bond-ordered-wave with fermions delocalized along the vertical bonds of the ladder in alternating symmetric/anti-symmetric orbitals, resembling an orbital AFM_x . Our numerics show that there are additional critical lines that separate this small-flux region from either the TCP lobes at higher flux, or the orbital PM at higher energy imbalances (see Figs. 8). As supported by the

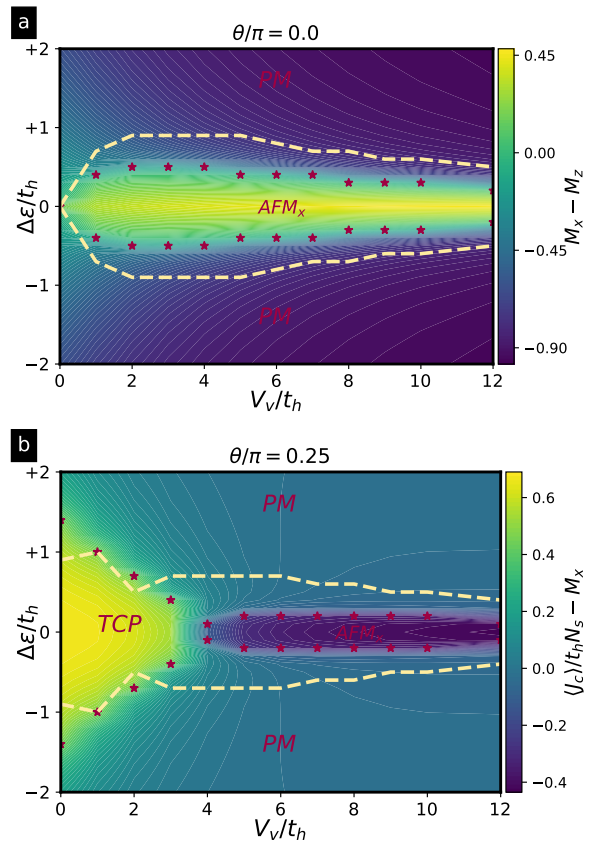


FIG. 11. **Phase diagram in the plane $(V_v, \Delta\varepsilon)$ for fixed flux:** (a) The phase diagram for $\theta = 0.0$ displays two regions hosting a long-range-ordered anti-ferromagnetic phase (AFM_x), and a paramagnetic phase (PM). (b) The phase diagram for $\theta = 0.25\pi$ displays a region hosting a topological crystalline phase (TCP), a long-range-ordered anti-ferromagnetic phase (AFM_x), and a paramagnetic phase (PM). The horizontal axis represents the the ratio of interaction to the tunneling strength, whereas the vertical axis corresponds to the ratio of the energy imbalance to the tunneling strength. The red stars (yellow dashed lines) show the critical points found from DMRG (self-consistently mean-field) numerics. These points are plotted the ratio of on top of the contour plot of the difference between the ferro and anti-ferro order parameters for (a) and of the chiral current for (b)

numerical results presented in the following paragraphs, this intermediate region hosts AFM_x long-range order due to SSB of a global \mathbb{Z}_2 invariance. To accurately extract the critical points between the AFM_x and PM, we calculate the staggered magnetization

$$M_x = \frac{1}{N_s} \sum_j (-1)^j \left(\langle c_{j,u}^\dagger c_{j,d} \rangle + \langle c_{j,d}^\dagger c_{j,u} \rangle \right), \quad (44)$$

which corresponds to the order parameter of the alternating bond density wave. The advantage of the strong-coupling perspective (31) is that one identifies the energy imbalance as the transverse magnetic field (32), and one can readily define the anti-ferromagnetic susceptibility as $\chi_{M_x} = \partial M_x / \partial \Delta\varepsilon$. In Fig. 10 (a), we present the staggered magnetization M_x for different system sizes. The crossing of the lines in the main

panel serve to obtain the critical point of the model for weak fluxes. As proved by the data collapse shown in the inset of Fig. 10 (a), the critical exponents correspond to those of the $(1+1)$ Ising universality class.

Moreover, we also want to address if the strong-coupling AFM_x phase, that appears for vanishingly-small fluxes, also sets for arbitrarily small values of the interaction strength V_v , or if a PM sets in before the AFM order takes on. For this aim, we will study the phase diagram sketched in Fig. 2 fixing the flux θ , and varying the imbalance $\Delta\epsilon$ and the interactions V_v , that permit us to explore different planes also the correlation effects at intermediate interactions. We set $\theta = 0.5\pi$ and $\theta = 0$, which correspond to the green and brown shaded planes of the schematic phase diagram of Fig. 2. Our numerical results for the phases of matter that appear in these planes are presented in Fig. 11, where we have used the self-consistent mean-field (yellow dashed line) and DMRG methods (red stars) to determine the critical lines. In the background, we present a contour plot that serves to as a guide to the eye to identify the different phases. As shown in the figure, the red stars obtained with a DMRG method based on finite MPS with bond dimension $\chi = 200$ yield a much better estimate of the critical lines that separate the different phases.

Let us start discussing the case of $\theta = 0.25\pi$ shown in Fig. 11(b). Here, one can distinguish three different phases: TCP, PM, and AFM_x . As can be observed in the figure for weak interaction, the Hartree-Fock and DMRG critical points separating the TCP and PM regions yield two critical lines similar to each other, although differences arise as the interactions are increased. Moreover, the weak-coupling limit can be understood as a ferromagnetic coupling between the two chains in the spin model description (as shown in the Appendix A). Along this line the central charge c is equal to 1.

We now move to the $\theta = 0$ case, which is represented in Fig. 11(a). In this case, one can readily observe that there is no TCP phase, but that the SSB AFM_x sets in at zero imbalance for vanishingly-small interactions. This result is consistent with the qualitative phase diagram of Fig. 2, and has very interesting consequences. While magnetism in standard Hubbard ladders only appear for small super-exchange couplings, making its detection with cold atoms rather challenging due to the required temperatures, the AFM_x order in the Creutz-Hubbard ladder for small fluxes appears at much-stronger scales, those set by the bare tunneling. This can be a very interesting starting point to introduce a non-zero doping and explore the interplay of magnetism and hole mobility in connection to fermionic mechanisms of superconductivity.

B. Strong Interactions

In Sec. IV B, we introduced an effective spin model (31) with Dzyaloshinskii-Moriya couplings in the limit of very strong interactions. This model is exactly solvable, and allowed us to predict a pair of critical lines (36) separating the orbital ferromagnet FM_y , anti-ferromagnet AFM_x , and paramagnet PM. We remark that these prediction are strictly valid in the limit where $V_v/t_h \rightarrow \infty$, and we should explore when

these predictions are valid for large, yet finite, interactions. In Fig. 12, we present the ground-state phase diagrams as a function of θ and $\Delta\epsilon$ for two values of the interactions $V_v = 10t_h$ and $V_v = 12t_h$, which correspond to the green and magenta shaded planes of the schematic phase diagram of Fig. 2. The red line, in both phase diagrams, represents the analytical critical line (36), whereas the white stars stand for the DMRG critical points, and the yellow dashed lines represent the mean-field predictions. One can see that the agreement of the strong-coupling critical lines with the DMRG data improves as the Hubbard interactions are increased, whereas the mean-field results overestimate the regions with long-range order. Note also that, by comparing Figs. 12 (a) and (b), one can see how the PM region grows significantly as the interactions are increased, in detriment of the long-range ordered phases, which is a consequence of the scaling of the super-exchange and Dzyaloshinskii-Moriya couplings (32) with the inverse of the Hubbard interactions. Let us now discuss in detail how we have characterised these phases and extracted the critical points.

In the background of Fig. 12, we present a contour plot for the difference of the orbital ferromagnetic and antiferromagnetic order parameters. Let us note that, in analogy to the anti-ferromagnetic case (44), one can define the orbital ferromagnetic parameter as

$$M_y = \frac{1}{N_s} \sum_j i \left(\langle c_{j,u}^\dagger c_{j,d} \rangle - \langle c_{j,d}^\dagger c_{j,u} \rangle \right), \quad (45)$$

which attains non-zero values for a purely-imaginary arrangement of bond densities. Note that such an arrangement is reminiscent of a set of alternating fermionic currents that flow vertically between the legs of the ladder. However, in contrast to the circulating chiral current (19), the corresponding vertical bare tunnelings are absent from the original Hamiltonian (1), and we would thus lack a continuity equation for such fermionic currents.

In order to avoid numerical problems due to the incomplete symmetry breaking of the magnetic order parameters M_x, M_y , we determine instead the corresponding structure factors

$$\begin{aligned} S_{T_y T_y}(k) &= \frac{1}{N_s^2} \sum_{i,j} e^{ika(i-j)} \langle T_i^y T_j^y \rangle, \\ S_{T_x T_x}(k) &= \frac{1}{N_s^2} \sum_{i,j} e^{ika(i-j)} |\langle T_i^x T_j^x \rangle|, \end{aligned} \quad (46)$$

where the orbital spin operators are defined in Eq. (30). The zero-momentum component of these structure factors yield the desired magnetizations in the thermodynamic limit $M_y = (S_{T_y T_y}(0))^{1/2}$, $M_x = (S_{T_x T_x}(0))^{1/2}$. In the insets of Figs. 13 (a) and (c), we show the two M_y, M_x order parameters, which attain a non-zero value for small energy imbalance, and for large $\theta = 0.65\pi$ and small $\theta = 0.1\pi$ magnetic fluxes, respectively. To locate the corresponding critical points delimiting the phase boundaries, we calculate the respective susceptibilities $\chi_{M_y} = \partial M_y / \partial \Delta\epsilon$, and $\chi_{M_x} = \partial M_x / \partial \Delta\epsilon$, which again show peaks whose FSS should determine the critical lines accurately. In the main panels of Fig. 13 (a) and (c), we can

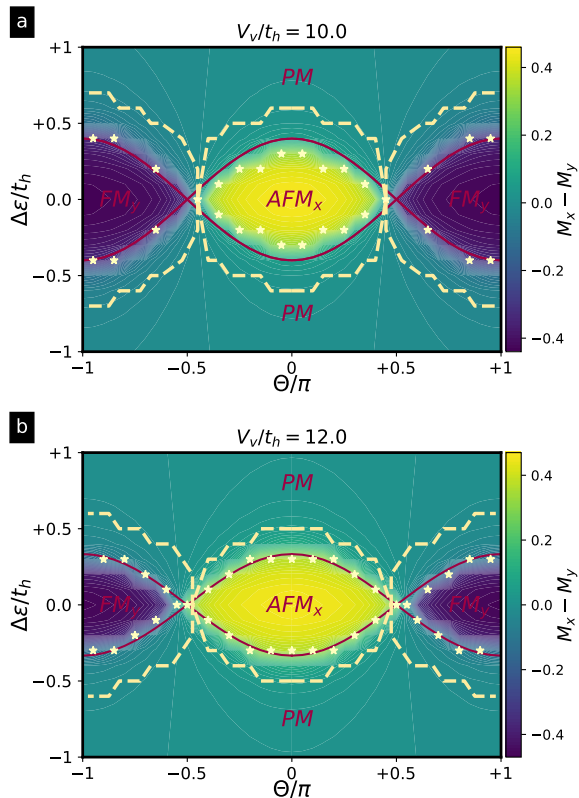


FIG. 12. **Phase diagram for strong interactions:** (a) $V_v = 10t_h$ and (b) $V_v = 12t_h$. The phase diagram displays a long-range ferromagnetic phase (FM_x), an anti-ferromagnetic phase (AFM_x), and a paramagnetic phase (PM). The horizontal axis represents the flux, whereas the vertical axis corresponds to the ratio of the energy imbalance to the tunneling strength. The red line shows the transition points (36) of the effective spin model with D-M interaction in strong coupling limit (31). The yellow stars show the critical points found by DMRG. Instead the shaded yellow lines shown the critical points from the self-consistently mean-field. The background contour plot represents the difference between the ferro and anti-ferro order parameters.

see how the susceptibilities peak at symmetric values of the zero-imbalance axis, and how these peaks grow with the lattice size. The numerical results shown in Figs. 13 (b) and (d) show that the susceptibility peaks agree considerably well with the analytical predictions already for these finite interactions and ladder lengths.

In Fig. 14, we show that the indicator for the phase transition FM-AFM is the chiral current and the chiral susceptibility.

C. Entanglement spectroscopy

Thus far, we have used a conventional condensed-matter approach to characterise the phase diagram of the model, which is based on exploiting currents, susceptibilities, and correlation functions to identify phases with long-range order or symmetry protected topological phases. In this section,

we follow an alternative approach based on the ground-state entanglement to understand the phase diagram of the model.

Among the various existing measures of entanglement on a bipartite scenario [171], we compute the entanglement spectrum and the entanglement entropy that enjoy a privileged status within the realm of quantum many-body system [172]. As regards the first one, we define a bipartition of the system, and write the ground-state as $|\psi_{g.s.}\rangle = \sum_n \lambda_n |\psi_n\rangle_L |\psi_n\rangle_R$, where L and R are two subsystem, and $\{\lambda_n\}$ are the corresponding Schmidt coefficients. The entanglement spectrum is defined as the set of all the Schmidt coefficients in logarithmic scale $\epsilon_n = -2 \log(\lambda_n)$, and it can be directly extracted from the MPS calculations. As originally pointed out in [173], in the context of the characterization of the Haldane phase of Heisenberg-type magnets, the degeneracy of the entanglement spectrum identifies the symmetry protecting topological phase.

It has been established that the entanglement spectrum is degenerate for symmetry-protected topological phases [174–176]. In particular, this degeneracy is robust against symmetric perturbations as long as the many-body gap of the system remains open. In Fig. 15 (a), we present the entanglement spectrum for the Creutz-Hubbard model for different interactions V_v and fluxes θ . As shown in Fig. 15 (b) (yellow column), the entanglement spectrum in the TCP phase is clearly doubly degenerate, whereas in the PM, FM_x and AFM_x phases such a degeneracy of all eigenvalues is lost (green columns). This supports our claim about the topological nature of the wide region of the phase diagram labeled as TCP, and demonstrates that the topological crystalline phase survives to considerable strong interactions. In particular, in the left panel of Fig. 15 (b), we present the entanglement spectrum for weak interactions for different values of the imbalance $\Delta\epsilon$ and fluxes θ . We consider a bipartition in the middle of chain, for $\Delta\epsilon = 0$ and $\theta = 0.5\pi$. Increasing $\Delta\epsilon$ and decreasing θ , we enter in the AFM_x or in PM phase, and the entanglement spectrum is trivial and almost completely degenerate, as shown in the green columns.

As regards the block entanglement entropy, it is defined as

$$S(l) = -\text{Tr}(\rho_l \ln \rho_l), \quad (47)$$

where $\rho_l = \text{Tr}_{N_s-l}(|\epsilon_{g.s.}\rangle\langle\epsilon_{g.s.}|)$ is the reduced density matrix of the left block with l sites for bipartition of each leg of the ladder of N_s sites. Remarkably enough, not only the block entanglement serve as a probe of criticality due to its divergence at phase transition, but its scaling with system size also reveals the central charge c of the conformal field theory underlying the critical behavior [177–179]. For a critical system with open boundary conditions, the block entanglement entropy scales as

$$S(l) = \frac{c}{6} \ln \left(\frac{2N_s}{\pi} \sin \frac{\pi l}{N_s} \right) + C, \quad (48)$$

where we introduce a non universal constant C . Since such entanglement entropy can be easily recovered from our MPS results, calculating the central charge of the different critical lines of our phase diagram can serve as an additional confirmation of our previous derivations. To explore the scaling

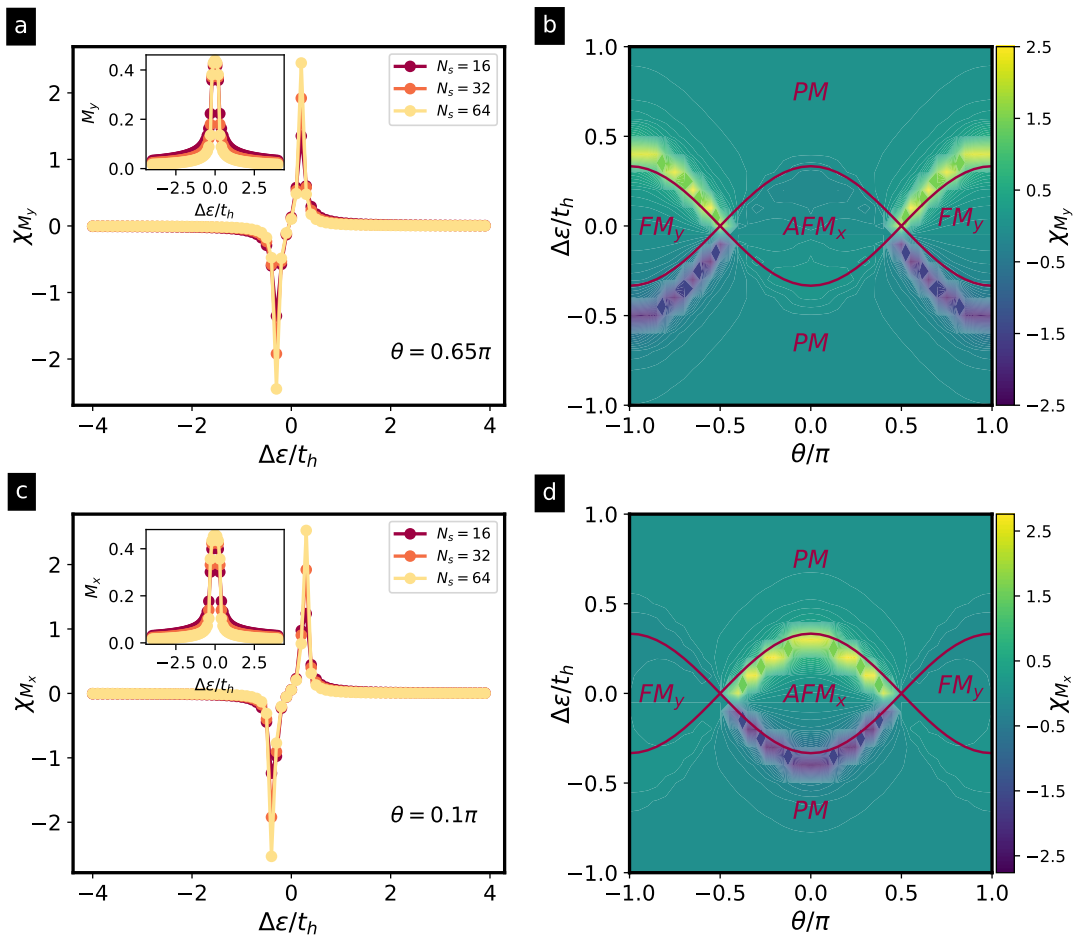


FIG. 13. **Magnetic susceptibilities for strong interactions:** (a) the divergence of χ_{M_y} with growing system size indicate the phase transition between FM_y and PM phases for a cut of phase diagram at $V_v = 10t_h$ and $\theta = 0.65\pi$. (b) The contour plot of χ_{M_y} for system size $N_s = 64$ distinguishes two FM_y lobes. The red line shows the analytical critical points (36) of the effective spin model (31), strictly valid for infinitely-large Hubbard interactions. (c) the divergence of χ_{M_x} with growing system size indicates the phase transition between AFM_x and PM phases for $V_v = 10t_h$ and $\theta = 0.1\pi$. (d) The contour plot of χ_{M_x} for system size $N_s = 64$ delimits the AFM_x phase. The red line shows the analytical critical points (36).

region of the quantum phase transition between topological and trivial band insulators, we represent in Fig. 15 (c) the critical entanglement entropy as a function of the so-called chord length $D(l, N_s) = (2N_s/\pi) \sin(\pi l/N_s)$, along the critical lines in 5 representative cases. For the TCP-PM transition the central charge value agrees with $c = 1$. This result can be understood well in the weakly interesting limit. In this regime, the Creutz-Hubbard model for generic flux can be understood as two coupled Ising chains, as shown in the Appendix A. In the limit of π -flux, the model is mapped to a couple of Ising chains in transverse magnetic field. Accordingly, the corresponding CFT should have central charge of $c = 1/2 + 1/2 = 1$ such that we would expect the scaling $S(l) = (1/6) \ln[(2N_s/\pi) \sin(\pi l/N_s) + a]$. In Fig. 15 (c), we also show that prediction are confirmed also for various fluxes.

For the strongly interacting regime, we showed in previous sections that the FM_y -PM and AFM_x -PM transitions can be accounted for by an XY model with D-M interaction. In

the limit of $\theta = \pi$, or $\theta = 0$, the model becomes a single Ising model in a transverse field. Accordingly, the corresponding CFT should have a central charge of $c = 1/2$, and $S(l) = \frac{1}{12} \ln[(\frac{2N_s}{\pi}) \sin(\frac{\pi l}{N_s})] + C$. In contrast to the previous case, the critical phenomena is governed by the CFT of single Majorana fermion with central charge $c = 1/2$.

Finally, in the intermediate interacting regime we argue that the relevant physics to understand the TI-FM phase transition is by approximating a complicated non standard model. In Fig. 15 (c), we show the entanglement entropy between the N -physical sites in the original basis and therefore measure $S(l) = \frac{1}{12} \ln[(\frac{2N_s}{\pi}) \sin(\frac{\pi l}{N_s})] + C$ for a system of length N_s with a central charge of $c = 1/2$.

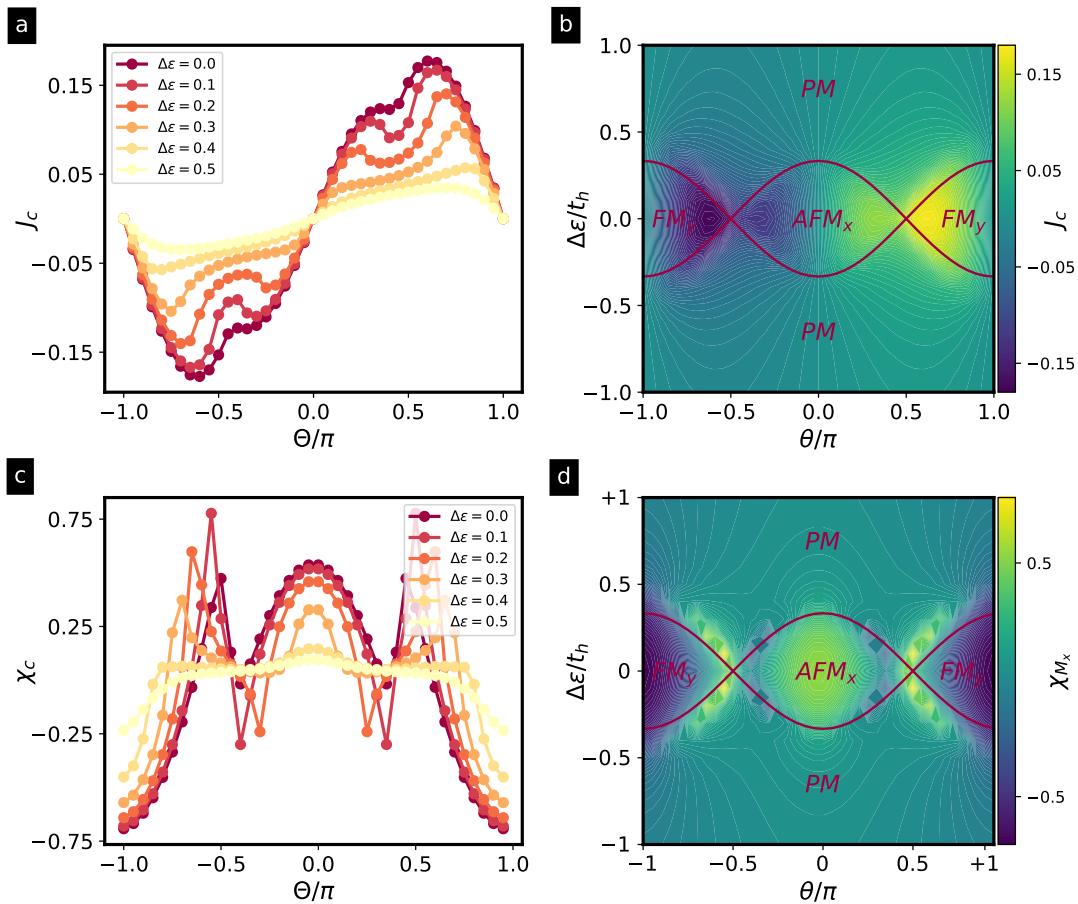


FIG. 14. **Chiral flows for strong interactions:** (a) Chiral current as a function of the magnetic flux for different energy imbalances $\Delta\epsilon$ and $V_y = 12t_h$. (b) The contour plot of the the chiral current qualitatively distinguishes the two phases. The red line shows the transition points of the effective spin model with D-M interaction in strong coupling limit (31). (c) Divergence of chiral susceptibility for different imbalance $\Delta\epsilon$ that indicates the phase transition between FM_y - AFM_x phases. (d) The maximum of χ_c that delimit the FM_y and AFM_x lobes.

VI. COLD-ATOM RAMAN LATTICE SCHEME

As outlined in the introduction, despite the fact that laser-cooled gases of neutral atoms move at velocities well below the speed of light [180], these systems yield an ideal platform for the quantum simulation [25] of relativistic QFTs [37]. Following the perspectives of lattice field theories, one need not look for cold-atom quantum simulators directly described by continuum QFTs (15), but instead look for a lattice model with critical points around which a long-wavelength description coincides with the target relativistic QFT. In this section, we describe a scheme based on cold atoms in optical Raman lattices for the quantum simulation of the Creutz-Hubbard ladder under an arbitrary flux (1)-(2). As emphasized previously, such a quantum simulator would provide the first experimental realization of Lorentz-violating terms (16) studied in the context of the SME [4–6], and combined with four-Fermi interactions of the Gross-Neveu type.

We note that the fermionic Creutz ladder has been recently realized in experiments with two-orbital ultracold-atoms in shaken optical lattices [181, 182]. In principle, interaction

effects could be explored by including more hyperfine states. Note, however, that such interacting models would likely correspond to a spin-full version of the Creutz ladder with short-range Hubbard-type interactions (see Fig. 1 (e)), which is different from the target model (1)-(2). To build the desired quantum simulator, the scheme proposed in Ref. [131] exploits the idea of synthetic dimensions [114] by mapping the ladder legs to a couple of hyperfine atomic states from the groundstate manifold [91, 95]. The attractive feature of this scheme is that the interactions along the vertical direction (2) in Fig. 1 (g), the so-called synthetic dimension, are mapped onto contact Hubbard interactions, which are readily implemented by the s -wave scattering of two ultracold atoms trapped in the same site of the optical lattice [71, 183].

Synthetic dimensions have been successfully exploited for the quantum simulation of rectangular ladders under a background magnetic field. The associated magnetic flux across the square plaquettes of the ladder can be simulated by a local Raman transition between the two hyperfine states [115, 184, 185], which induces a Peierls-substituted vertical tunneling that connects the upper and lower legs of the ladder

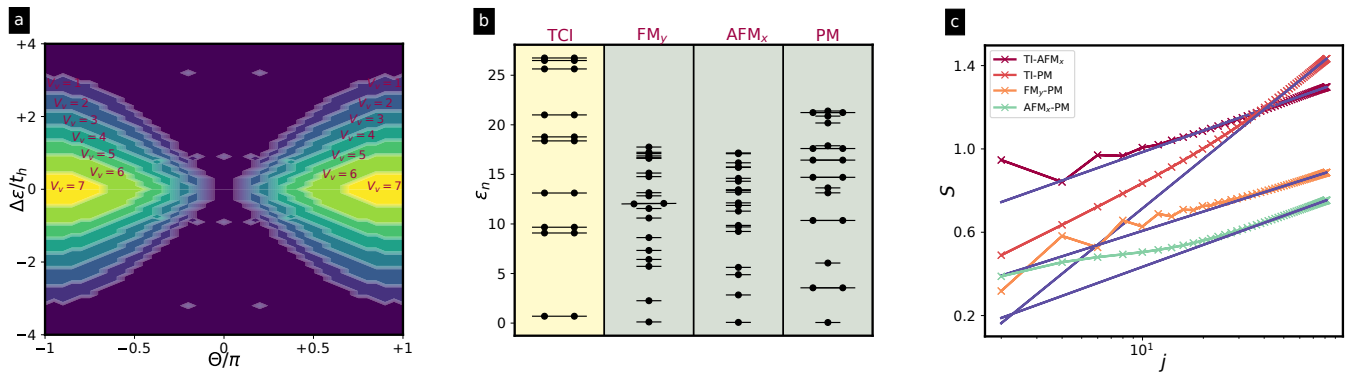


FIG. 15. **Entanglement spectrum and entanglement entropy:** (a) Degeneracies of the entanglement spectrum in the $(\theta, \Delta\epsilon)$ plane for different interactions. We show that the region in which the entanglement spectrum shows an exact two-fold degeneracy, and thus corresponds to the topological crystalline phase, gets reduced by increasing the interactions. (b) Low-lying eigenvalues of the entanglement spectrum for the different phases. For a ladder of length $N_s = 128$, and for a half-chain bipartition of the chain. Only the TCP phase displays an exact two-fold degeneracy. (c) Entanglement entropy for a l -sites block reduced density matrix ρ_l obtained from a ladder of length $N_s = 128$. The blue, red, and yellow crosses correspond to the data for the critical points. The solid lines correspond to the fittings with the conformal field theory predictions (48), where c is the central charge. The fitted central charges are $c = 1.02$, $c = 0.503$, and $c = 0.49$, respectively.

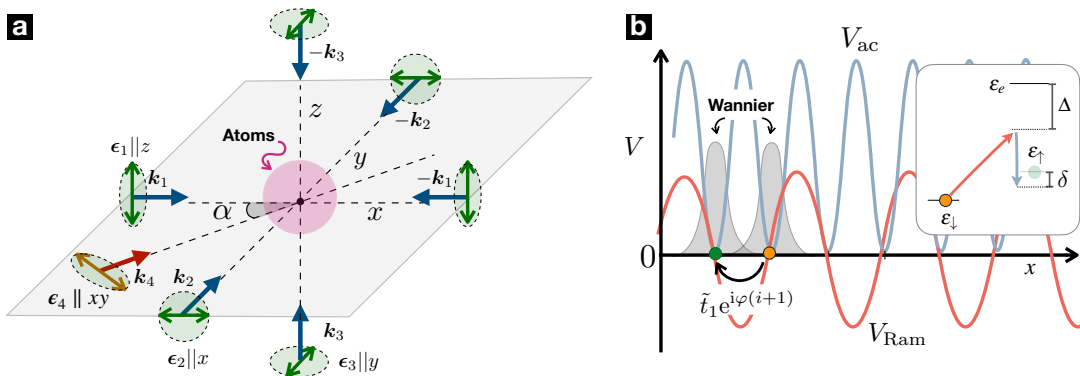


FIG. 16. **Scheme of the optical Raman potential for the quantum simulation of the Creutz-Hubbard ladder:** (a) A cloud of atoms, represented by a pink shaded sphere, is subjected to three pairs of counter-propagating laser beams with mutually-orthogonal polarisations, here depicted with blue arrows, which create a cubic optical lattice. A fourth laser beam, represented by a red arrow, propagates in the xy plane with an angle α with respect to the x axis, sharing the polarization with the standing wave along that axis $\epsilon_4 \parallel \epsilon_1$. The interference of the standing- and traveling-wave drives a two-photon Raman transition between two hyperfine states when the beatnote is tuned close to the resonance of the latter $\Delta\omega = \omega_1 - \omega_4 = \epsilon_\uparrow - \epsilon_\downarrow - \delta = \omega_0 - \delta$ by virtually populating a highly-off-resonant excited state $\delta \ll \omega_0 \ll \Delta$ (see the inset of (b)). As shown in (b), due to this interference, this Raman term V_{Ram} has a doubled period with respect to the static optical lattice V_{ac} . The atoms trapped at the minima of this optical lattice do not see any intensity of the Raman beams, and there is no local transitions. On the other hand, the overlap between neighboring Wannier functions of opposite spin mediated by this Raman potential can lead to a spin-flipping tunneling of strength \tilde{t}_1 with a site-dependent phase φ , which is controlled by the tilting angle α .

(see Fig. 1 (c)). For the Creutz ladder, the situation is complicated further due to the cross-link nature of the inter-leg tunnelings (see Fig. 1 (g)). As proposed in [131], these cross-linked terms could be implemented by a Raman-assisted tunneling scheme [186] that activates a spin-flipping tunneling against the energy penalty of a linear lattice tilt. Note that, as the cross-link tunnelings take place in both directions, i.e. $(u, i) \rightarrow (d, i+1)$ and $(d, i) \rightarrow (u, i+1)$, the scheme does not require the use of state-dependent lattices as occurs for the simulation of the Hofstadter model [186], minimising in this way the expected heating due to residual spontaneous emission in the fermionic Raman couplings. The implementa-

tion of the horizontal tunnelings (see Fig. 1 (g)) requires a different mechanism to assist the spin-conserving tunneling while imprinting an effective Peierls' phase. In the scheme of Ref. [131], this is provided by an additional shallower lattice potential with a doubled wavelength, the intensity of which is periodically modulated. This allows for a Floquet-assisted tunneling mechanism with the desired Peierls' phase, mimicking the role of the external magnetic flux.

We note that the combination of Floquet-assisted tunneling with Hubbard interactions, as would be required for this full quantum simulator of the Creutz-Hubbard ladder [131], may present limitations due to a heating mechanism where

the atoms get excited by resonantly absorbing quanta from the periodically-driven radiation [132, 187, 188]. Although there has been promising progress in the minimization of this heating in specific optical-lattice implementations [189–192], it would be desirable to come up with a different scheme that implements the Peierls phases in the cross-linked geometry. The goal of this section is to present such a scheme.

We show that the recent progress in synthetic spin-orbit coupling with cold atoms in the so-called optical Raman potentials [42] can be exploited for the full quantum simulator of the Creutz-Hubbard ladder (1)-(2). In these schemes, one combines periodic ac-Stark shifts from a standing wave with Raman potentials that stem from the interference of lasers in standing- and traveling-wave configurations. As discussed in more detail below, when the beatnote of the standing- and traveling-wave laser beams is tuned close to the spin-flip transition frequency, the Raman cross terms do not drive local spin flips [193–197], but instead assist a spin-flipping tunneling that can be used to simulate spin-orbit coupling [150–153]. Although these Raman schemes may also be limited by residual photon scattering from the off-resonant excited state, the associated heating is not as severe as that of fermions trapped in state-dependent lattices since, if the available laser intensity is not the limiting factor, this heating can be minimised by working with larger Raman detunings Δ with respect to the excited state (see inset of Fig. 16 (b)). In any case, one may also consider using lanthanide [120, 198–200] or alkali-earth [121, 122, 153] atoms in order to minimise it further.

Let us now describe in detail how these periodic optical potentials can be exploited for the specific quantum simulation of the Creutz-Hubbard ladder (1)-(2), and how to tune the value of the synthetic magnetic flux θ . In contrast to the scheme that realizes Rashba- or Dirac-type spin-orbit coupling [42], we consider a configuration where the traveling wave does not propagate orthogonally to the x -axis standing wave, but instead at an angle α (see Fig. 16 (a)). In addition, we consider two additional standing waves with orthogonal polarisations along the remaining spatial directions, which will lead to periodic optical potentials along the y and z axes. In the regime where the lasers are far detuned with respect to an excited state, this creates a periodic optical potential for the atoms in two hyperfine states $\sigma \in \{\uparrow, \downarrow\}$, namely

$$V = \sum_{\alpha} \frac{V_{0,\alpha}}{2} \cos^2(\mathbf{k}_{\alpha} \cdot \mathbf{x}) \mathbb{I}_2 + \frac{\tilde{V}_0}{2} \cos(\mathbf{k}_1 \cdot \mathbf{x}) e^{i(\mathbf{k}_4 \cdot \mathbf{x} - \Delta \omega t)} \sigma^+ + \text{H.c.}, \quad (49)$$

where $\sigma^+ = |\uparrow\rangle\langle\downarrow|$. Here, $V_{0,\alpha}$ are the amplitudes of the ac-Stark shifts induced by pairs of counter-propagating laser beams along each of the axes $\mathbf{k}_{\alpha} = k_{\alpha} \mathbf{e}_{\alpha}$ with $\alpha \in \{1, 2, 3\} \equiv \{x, y, z\}$. These pairs of laser beams have mutually orthogonal polarizations, such that the interference patterns along each axis in the first term of Eq. (49) can be tuned independently, and thus corresponds to a standard cubic optical lattice. Additionally, \tilde{V}_0 is the amplitude of the two-photon Raman transition, whereby the spin state gets flipped by virtually populating an excited state. As shown in the inset of (see Fig. 16 (b)), this transition involves absorbing a photon from the travelling wave, which propagates along $\mathbf{k}_4 = k_4 \cos \alpha \mathbf{e}_1 + k_4 \sin \alpha \mathbf{e}_2$,

and subsequently re-emitting it in the standing wave. This leads to a beatnote of frequency $\Delta \omega = \omega_4 - \omega_1$ that can drive the spin flips when tuned close to the resonance $\Delta \omega \approx \omega_0$. A crucial aspect of this type of schemes, which can already be appreciated at this stage, is that the period of the spin-flipping potential is doubled with respect to that of the static optical lattice (see Fig. 16 (b)). As such, the atoms residing at the minima of the latter do not see any Raman intensity that would drive local transitions, but it is only in the spin-flip tunneling where this Raman term contributes.

As noted at the beginning of this section, these systems can be described by the following non-relativistic QFT

$$H = \int d^3x \sum_{\sigma, \sigma'} \Phi_{\sigma}^{\dagger}(\mathbf{x}) \left(-\frac{\nabla^2}{2m} + \langle \sigma | V(\mathbf{x}) | \sigma' \rangle \right) \Phi_{\sigma'}(\mathbf{x}) + \int d^3x \int d^3x' \sum_{\sigma, \sigma'} \Phi_{\sigma}^{\dagger}(\mathbf{x}) \Phi_{\sigma'}^{\dagger}(\mathbf{x}') \frac{2\pi a_s}{m} \delta(\mathbf{x} - \mathbf{x}') \Phi_{\sigma'}(\mathbf{x}') \Phi_{\sigma}(\mathbf{x}), \quad (50)$$

where m is the mass of the atoms, and a_s the s -wave scattering length for the low-energy two-body collisions. We have introduced the fermionic field operators $\Phi_{\sigma}^{\dagger}(\mathbf{x}), \Phi_{\sigma}(\mathbf{x})$ that create-annihilate an atom at position \mathbf{x} with internal state σ . Note that these fields differ from the relativistic ones (10), which will be recovered in the long-wavelength limit of the lattice model. To obtain such a lattice description, we consider the regime of deep optical lattices $V_{0,\alpha} \gg E_{R,\alpha} = k_{\alpha}^2/2m$, where the atoms are tightly confined to the minima of the periodic blue-detuned optical lattice (see Fig. 16 (b)). The lattice sites thus correspond to $\mathbf{x}_i^0 = \sum_{\alpha} \frac{\lambda_{\alpha}}{2} (i_{\alpha} + \frac{1}{2}) \mathbf{e}_{\alpha}$, where $\lambda_{\alpha} = 2\pi/k_{\alpha}$ are the wavelengths of the standing-wave laser beams, and $i_{\alpha} \in \mathbb{Z}_{N_s}$. We now express the fields in the Wannier basis

$$\Phi_{\sigma}(\mathbf{x}) = \sum_i w(\mathbf{x} - \mathbf{x}_i^0) f_{i,\sigma}, \quad \Phi_{\sigma}^{\dagger}(\mathbf{x}) = \sum_i w(\mathbf{x} - \mathbf{x}_i^0) f_{i,\sigma}^{\dagger}, \quad (51)$$

where $w(\mathbf{x} - \mathbf{x}_i^0)$ are the Wannier functions localised around each minima \mathbf{x}_i^0 of the optical potential, and $f_{i,\sigma}^{\dagger}, f_{i,\sigma}$ is a set of dimensionless lattice operators that describe the creation-annihilation of fermions in the lowest band of the optical lattice. Substituting these expressions in the QFT (50), one obtains a lattice model with parameters that depend on the overlaps of these Wannier functions. These parameters decay exponentially fast with the distance, and are typically restricted to on-site and nearest-neighbor terms [71, 183].

This lattice model is composed of spin-conserving terms

$$H_{\text{sc}} = \sum_i \left(\sum_{\sigma, \alpha} \left(-t_{\alpha} f_{i,\sigma}^{\dagger} f_{i+\mathbf{e}_{\alpha}, \sigma} + \text{H.c.} \right) + \sum_{\sigma \neq \sigma'} \frac{U_{\uparrow\downarrow}}{2} n_{i,\sigma} n_{i,\sigma'} \right), \quad (52)$$

where $n_{i,\sigma} = f_{i,\sigma}^{\dagger} f_{i,\sigma}$, and we have introduced the tunnelings

$$t_{\alpha} = \frac{4}{\sqrt{\pi}} E_R \left(\frac{V_{0,\alpha}}{E_R} \right)^{\frac{3}{4}} e^{-2\sqrt{\frac{V_{0,\alpha}}{E_R}}}, \quad (53)$$

assuming that the standing waves have the same wavelength

$\lambda_\alpha = 2\pi/k, \forall \alpha$. Likewise, the Hubbard interaction reads

$$U_{\uparrow\downarrow} = \sqrt{\frac{8}{\pi}} ka_s E_R \left(\frac{V_{0,1} V_{0,2} V_{0,3}}{E_R^3} \right)^{\frac{1}{4}}. \quad (54)$$

By setting $V_{0,2}, V_{0,3} \gg V_{0,1} \gg E_R$, the tunnelings along the y and z axes (53) are inhibited $t_2, t_3 \ll t_1$, and we obtain an effective Fermi-Hubbard model in one spatial dimension. Note that, in addition to these spin-conserving terms, there will also be local terms corresponding to on-site energies that can be approximated by an overall quadratic trapping potential.

In addition to these contributions, we have the spin-flipping Raman potential (49) that stems from the interference of the standing and traveling waves along the x axis, and will lead to spin-flipping terms in the lattice model. In this case, the local terms are not simply an on-site potential, as discussed in

the previous paragraph but, instead, describe processes where an atom tightly confined to a minimum of the optical potential experiences a Raman transition that flips its internal state $|\uparrow\rangle \leftrightarrow |\downarrow\rangle$. This type of terms can indeed be exploited to implement the synthetic dimensions discussed in the introduction [115, 184, 185]. Note that these terms correspond to a vertical tunneling within the synthetic ladder, and would thus spoil the cross-linked nature of the Creutz-ladder of Fig. 1 (g). Fortunately, the corresponding Wannier integrals vanish since the Raman potential is odd with respect to each lattice site while the Wannier functions are even (see Fig. 16 (b)),

$$\int d^3x w(\mathbf{x} - \mathbf{x}_i^0) \frac{\tilde{V}_0}{2} \cos(\mathbf{k}_1 \cdot \mathbf{x}) e^{i\mathbf{k}_4 \cdot \mathbf{x}} w(\mathbf{x} - \mathbf{x}_i^0) = 0. \quad (55)$$

The leading spin-flipping terms are thus described by tunnelings along the x axis that stem from the following overlaps

$$\int d^3x w(\mathbf{x} - \mathbf{x}_i^0) \frac{\tilde{V}_0}{2} \cos(\mathbf{k}_1 \cdot \mathbf{x}) e^{i\mathbf{k}_4 \cdot \mathbf{x}} w(\mathbf{x} - \mathbf{x}_j^0) \approx \frac{\tilde{V}_0}{2} e^{-\frac{1}{4}mv|\mathbf{x}_i^0 - \mathbf{x}_j^0|^2} \cos\left(\frac{1}{2}\mathbf{k}_1 \cdot (\mathbf{x}_i^0 + \mathbf{x}_j^0)\right) e^{\frac{i}{2}\mathbf{k}_4 \cdot (\mathbf{x}_i^0 + \mathbf{x}_j^0)}, \quad (56)$$

where we have performed a Gaussian approximation around the minima of each lattice site, where the lattice potential can be approximated by a harmonic oscillator of frequency $\nu = 2\sqrt{V_{0,1}E_R}$. As occurs for the spin-conserving terms, these tunnelings decay rapidly with the distance, such that we can restrict to nearest-neighbors. In this case, the overlaps display a crucial alternation of the sign, $\cos\left(\frac{1}{2}\mathbf{k}_1 \cdot (\mathbf{x}_i^0 + \mathbf{x}_{i+\mathbf{e}_1}^0)\right) = \exp\{i\pi(i_1 + 1)\}$, which has been exploited to simulate synthetic spin-orbit coupling [150–152]. The novelty of our scheme is that the non-orthogonal propagation of the traveling wave shown in Fig. 16 (a) allows us to pick up an arbitrary phase factor that shall also play a crucial role, namely $\exp\left\{\frac{i}{2}\mathbf{k}_4 \cdot (\mathbf{x}_i^0 + \mathbf{x}_{i+\mathbf{e}_1}^0)\right\} = \exp\{i\eta(i_1 + 1)\}$, where

$$\eta = \frac{k_4}{k_1} \cos \alpha. \quad (57)$$

Note that there is also a dependence of this phase factor on the particular lattice site along the y axis, but the negligible tunnelings along this direction allow us to gauge it away without changing the dynamics.

Let us now tune the Raman beatnote slightly off-resonance with respect to the internal transition $\Delta\omega = \omega_0 - \delta$, where the detuning is constrained to $\delta \ll \omega_0$. Considering the discussion in the previous paragraph, and working in a rotating frame, we find that the Raman potential leads to the following spin-flipping tunnelings and energy imbalance

$$H_{\text{sf}} = \sum_i \tilde{t}_1 \left(e^{i\varphi(i_1+1)} f_{i,\uparrow}^\dagger f_{i+\mathbf{e}_1,\downarrow} + e^{-i\varphi(i_1+1)} f_{i,\downarrow}^\dagger f_{i+\mathbf{e}_1,\uparrow} \right) + \text{H.c.} \\ + \sum_i \frac{\delta}{2} \left(f_{i,\uparrow}^\dagger f_{i,\uparrow} - f_{i,\downarrow}^\dagger f_{i,\downarrow} \right), \quad (58)$$

where we have introduced the following parameters

$$\tilde{t}_1 = \frac{\tilde{V}_0}{2} e^{-\frac{\pi^2}{4} \sqrt{\frac{V_{0,1}}{E_R}}}, \quad \varphi = \pi(1 + \eta). \quad (59)$$

The final step to define our quantum simulator is to map the fermionic operators of the Creutz-Hubbard ladder (1)-(2) via a synthetic dimension to the cold-atom operators

$$c_{i,u} = e^{-i\frac{\varphi}{2}(i+1)} f_{i,\uparrow}, \quad c_{i,d} = e^{+i\frac{\varphi}{2}i} f_{i,\downarrow}, \quad (60)$$

such that the cold-atom lattice model in Eqs. (52)-(58) maps directly onto the Creutz-Hubbard ladder (1)-(2) with the following identification of microscopic parameters

$$t_h = t_1, \quad t_d = -\tilde{t}_1, \quad \Delta\varepsilon = \delta, \quad \theta = \varphi, \quad V_v = U_{\uparrow\downarrow}. \quad (61)$$

Note that the various observables discussed in our study of the Creutz-Hubbard ladder may be modified by virtue of the $U(2)$ gauge transformation (60). One should thus identify the correct cold-atom operators that contain the relevant information about the groundstate phases of the Creutz-Hubbard ladder.

It follows from our discussion that all of these parameters can be tuned independently. The horizontal tunneling is controlled by the intensity of the standing-wave lasers via Eq. (53). If, on the other hand, one modifies the intensity of the travelling-wave laser, only the spin-flip tunneling will change (59), which translates into a modification of the cross-link tunneling of the Creutz-Hubbard ladder (see Fig. 1 (g)). In order to modify the synthetic magnetic flux independently, Eqs. (57)-(59) show that one must either modify the angle α of propagation of the travelling wave. Similarly, the energy imbalance is controlled by the beatnote detuning, which can be readily modified by changing the frequency of travelling-wave laser. Finally, the Hubbard interactions can be tuned by exploiting a Feshbach resonance in the scattering length (54).

VII. CONCLUSIONS AND OUTLOOK

In this work, we have described the connection between Lorentz-violating four-Fermi QFTs and models of correlated topological crystalline phases. By focusing on the Creutz-Hubbard ladder for arbitrary magnetic flux, we have presented a thorough analysis based on analytical and numerical tools, showing that, as a consequence of the violation of Lorentz invariance, persistent chiral currents can coexist with strong correlations in the topological crystalline phase. We have discussed in detail the phase diagram of the model and the nature of the phase transitions, showing that the chiral current and its susceptibility provide relevant information, which can be complemented with other observables and entanglement-related quantities. We have also discussed an experimental scheme based on ultra-cold Fermi gases in tilted Raman lattices for the quantum simulation of these phenomena. We refer the reader again to Sec. II C, where all these results have been summarised. We would like to conclude by noting that our work constitutes an example of the useful dialogue and exchange of ideas between the high-energy physics, condensed matter, quantum information, and quantum optics, hopefully stimulating further cross-disciplinary efforts in the future. From the above results, we are convinced that the synthetic Creutz-Hubbard ladder with generic flux can become a work horse in the theoretical and experimental study of correlated topological phases of matter, connecting high-energy physics and condensed matter, and proving a clear path to for its implementation via ultra-cold atoms. This would provide the first experimental realization of Lorentz-violating QFTs within the Standard Model extension.

As an outlook, it would be very interesting to exploit these cross-disciplinary approaches to understand the physics of the Creutz-Hubbard ladder at generic flux, and thus the Gross-Neveu model extension, as one moves away from half-filling and thus explores finite fermion densities in the continuum QFT. It will also be interesting to explore real-time dynamical effects in this model, in particular in connection with anomalies, the circulating chiral current, and the underlying violation of Lorentz symmetry. This would require to upgrade the flux θ to a dynamical variable with its own dynamics described by a $U(1)$ lattice gauge theory, following a similar gauging as in the case of a \mathbb{Z}_2 gauge group [201]. As discussed for other lattice models in [202, 203], \mathbb{Z}_N discrete gauge groups could also be explored as a proxy for the $U(1)$ ladder gauge theory. It will be very interesting to study the interplay of this gauge theory with the topological crystalline insulator and its associated edge states. We note that both the finite-density and real-time phenomena provide very challenging problems where the advantage of the quantum simulator could be exploited. Finally, it would also be interesting to explore how other terms within the SME can be incorporated in a lattice model, and how this model could be realised in experiments of ultra-cold atoms.

ACKNOWLEDGEMENTS

ICFO group acknowledges support from: ERC AdG NOQIA; Agencia Estatal de Investigación (R&D project CEX2019-000910-S, funded by MCIN/AEI/10.13039/501100011033, Plan National FIDEUA PID2019-106901GB-I00, FPI, QUANTERA MAQS PCI2019-111828-2, Proyectos de I+D+I Retos Colaboración RTC2019-007196-7); Fundació Cellex; Fundació Mir-Puig; Generalitat de Catalunya through the CERCA program, AGAUR Grant No. 2017 SGR 134, QuantumCAT U16-011424, co-funded by ERDF Operational Program of Catalonia 2014-2020; EU Horizon 2020 FET-OPEN OPTologic (Grant No 899794); National Science Centre, Poland (Symfonia Grant No. 2016/20/W/ST4/00314); Marie Skłodowska-Curie grant STREDCH No 101029393; “La Caixa” Junior Leaders fellowships (ID100010434) and EU Horizon 2020 under Marie Skłodowska-Curie grant agreement No 847648 (LCF/BQ/PI19/11690013, LCF/BQ/PI20/11760031, LCF/BQ/PR20/11770012, LCF/BQ/PR21/11840013). A.B. acknowledges support from the Ramón y Cajal program RYC-2016-20066, CAM/FEDER Project S2018/TCS- 4342 (QUITEMADCM), and PGC2018-099169-B-I00 (MCIU/AEI/FEDER, UE).

Appendix A: Weak interactions and coupled Ising chains

In this appendix, we discuss more in detail the weak interacting limit $t_h \gg V_v$ of the Creutz-Hubbard ladder for generic flux, and in particular we will show how in this limit we can map the Creutz ladder as spin ladder.

We start from the free part of the Creutz-Hubbard Hamiltonian H_c defined in the eq.(1). Introducing the spinor notation and performing the transformation $c_j = (-i\sigma_z)^j \tilde{c}_j$, we obtain that the hopping along the two legs becomes now identical at the price of having site-dependent diagonal hopping terms that connect neighboring sites in opposite legs of the ladder:

$$H_C = \sum_j \tilde{c}_j^\dagger \left[-t_h I - t_d \cos\left(\frac{\theta}{2}(2j+1)\right) \sigma_x + t_d \sin\left(\frac{\theta}{2}(2j+1)\right) \sigma_y \right] c_{j+1} + \frac{\Delta\varepsilon}{4} \tilde{c}_j^\dagger \sigma_z \tilde{c}_j + \text{H.c.} \quad (\text{A1})$$

Introducing the following rung operators:

$$r_{j,1} = \frac{i^j}{\sqrt{2}} \left[i\tilde{c}_{j,u} + (-1)^j \tilde{c}_{j,d}^\dagger \right], \quad (\text{A2})$$

$$r_{j,2} = \frac{i^j}{\sqrt{2}} \left[\tilde{c}_{j,u} + (-1)^j \tilde{c}_{j,d}^\dagger \right],$$

Under this canonical transformation, the Hamiltonian is trans-

formed onto

$$\begin{aligned}
H_c = & \sum_{jn} \left[-t_h \left(r_{j+1,n}^\dagger r_{j,n} + H.c. \right) \right. \\
& + t_d \left((-1)^{j+1} i e^{i\frac{\theta}{2}(2j+1)} r_{j+1,n}^\dagger r_{j,n}^\dagger + H.c. \right) \\
& \left. + \frac{\Delta\epsilon}{4} \left(2r_{j,n}^\dagger r_{j,n} - 1 \right) \right] \quad (\text{A3})
\end{aligned}$$

In this particle-hole rung basis Eq. A2, we identify two independent subsystems which no longer display particle number conservation, but instead have parity conservation. A Jordan-Wigner transformation [204], namely,

$$r_{j,n}^\dagger = \prod_{i<j} (-\sigma_{i,n}^z) \sigma_{j,n}^+ = (r_{j,n})^\dagger \quad (\text{A4})$$

reveals the Ising nature of the two subsystems, and leads to a Hamiltonian that can be understood as a two-leg quantum spin ladder

$$\begin{aligned}
H_c = & \sum_{jn} \left[-t_h \left(\sigma_{j+1,n}^+ \sigma_{j,n}^- + H.c. \right) \right. \\
& + t_d \left((-1)^{j+1} i e^{i\frac{\theta}{2}(2j+1)} \sigma_{j+1,n}^+ \sigma_{j,n}^+ + H.c. \right) + \frac{\Delta\epsilon}{4} \sigma_{j,n}^z \left. \right]. \quad (\text{A5})
\end{aligned}$$

We now consider the model with Hubbard-like interactions

for the first time. In particular, we take a look at the regime of small interactions $V_v < t$ and study how these interactions alter the results of the non-interacting model. Applying the series of transformations presented above we obtain that the interaction term reads

$$\begin{aligned}
\hat{H}_{\text{Hub}} = & \frac{V_v}{2} \sum_j \left(\hat{r}_{j,1}^\dagger \hat{r}_{j,1} + \hat{r}_{j,2}^\dagger \hat{r}_{j,2} + i \hat{r}_{j,1}^\dagger \hat{r}_{j,2} \right. \\
& \left. - i \hat{r}_{j,2}^\dagger \hat{r}_{j,1} - 2 \hat{r}_{j,1}^\dagger \hat{r}_{j,1} \hat{r}_{j,2}^\dagger \hat{r}_{j,2} \right). \quad (\text{A6})
\end{aligned}$$

For half filling we have $\langle \hat{r}_{j,1}^\dagger \hat{r}_{j,2} - \hat{r}_{j,2}^\dagger \hat{r}_{j,1} \rangle = 0$, simplifying the Hamiltonian to

$$\hat{H}_{\text{Hub}} = \frac{V_v}{2} \sum_j \left(\hat{r}_{j,1}^\dagger \hat{r}_{j,1} + \hat{r}_{j,2}^\dagger \hat{r}_{j,2} - \hat{r}_{j,1}^\dagger \hat{r}_{j,1} \hat{r}_{j,2}^\dagger \hat{r}_{j,2} \right). \quad (\text{A7})$$

The Jordan-Wigner transformation translates this expression to a ferromagnetic coupling between the two spin models:

$$\hat{H}_{\text{Hub}} = \frac{V_v}{4} \sum_j \left(1 - \sigma_{j,1}^z \sigma_{j,2}^z \right). \quad (\text{A8})$$

In π -flux regime, the imbalanced Creutz-Hubbard model can be understood as two coupled quantum Ising chains. For weak interactions $V_v < t_h$, we can treat the mutual effect of chains on each other through an MF decoupling which renormalizes the original transverse magnetization term.

-
- [1] M. E. Peskin and D. V. Schroeder, *An Introduction to quantum field theory* (Addison-Wesley, Reading, USA, 1995).
- [2] V. A. Kostelecký and S. Samuel, *Phys. Rev. D* **39**, 683 (1989).
- [3] S. M. Carroll, J. A. Harvey, V. A. Kostelecký, C. D. Lane, and T. Okamoto, *Phys. Rev. Lett.* **87**, 141601 (2001).
- [4] D. Colladay and V. A. Kostelecký, *Phys. Rev. D* **58**, 116002 (1998).
- [5] V. A. Kostelecký, C. D. Lane, and A. G. M. Pickering, *Phys. Rev. D* **65**, 056006 (2002).
- [6] D. Colladay and V. Kostelecký, *Physics Letters B* **511**, 209 (2001).
- [7] D. Mattingly, *Living Reviews in Relativity* **8**, 5 (2005).
- [8] T. Pruttivarasin, M. Ramm, S. G. Porsev, I. I. Tupitsyn, M. S. Safronova, M. A. Hohensee, and H. Häffner, *Nature* **517**, 592 (2015).
- [9] S. Chadha and H. Nielsen, *Nuclear Physics B* **217**, 125 (1983).
- [10] E. Fradkin, *Field Theories of Condensed Matter Physics*, 2nd ed. (Cambridge University Press, 2013).
- [11] L. Landau, *Zh. Eksp. Teor. Fiz* **11**, 26 (1937).
- [12] K. G. Wilson and J. Kogut, *Physics Reports* **12**, 75 (1974).
- [13] R. Shankar, *Rev. Mod. Phys.* **66**, 129 (1994).
- [14] J. Bardeen, L. N. Cooper, and J. R. Schrieffer, *Phys. Rev.* **106**, 162 (1957).
- [15] Y. Nambu and G. Jona-Lasinio, *Phys. Rev.* **122**, 345 (1961).
- [16] Y. Nambu and G. Jona-Lasinio, *Phys. Rev.* **124**, 246 (1961).
- [17] P. W. Anderson, *Phys. Rev.* **130**, 439 (1963).
- [18] F. Englert and R. Brout, *Phys. Rev. Lett.* **13**, 321 (1964).
- [19] P. W. Higgs, *Phys. Rev. Lett.* **13**, 508 (1964).
- [20] A. H. Castro Neto, F. Guinea, N. M. R. Peres, K. S. Novoselov, and A. K. Geim, *Rev. Mod. Phys.* **81**, 109 (2009).
- [21] N. P. Armitage, E. J. Mele, and A. Vishwanath, *Rev. Mod. Phys.* **90**, 015001 (2018).
- [22] X.-L. Qi and S.-C. Zhang, *Rev. Mod. Phys.* **83**, 1057 (2011).
- [23] I. Bloch, J. Dalibard, and S. Nascimbène, *Nature Physics* **8**, 267 (2012).
- [24] R. Blatt and C. F. Roos, *Nature Physics* **8**, 277 (2012).
- [25] R. P. Feynman, *Int. J. Theor. Phys.* **21**, 467 (1982).
- [26] L. Tarruell, D. Greif, T. Uehlinger, G. Jotzu, and T. Esslinger, *Nature* **483**, 302 (2012).
- [27] L. Duca, T. Li, M. Reitter, I. Bloch, M. Schleier-Smith, and U. Schneider, *Science* **347**, 288 (2015).
- [28] C. Schweizer, F. Grusdt, M. Berngruber, L. Barbiero, E. Demler, N. Goldman, I. Bloch, and M. Aidelsburger, *Nature Physics* **15**, 1168 (2019).
- [29] A. Mil, T. V. Zache, A. Hegde, A. Xia, R. P. Bhatt, M. K. Oberthaler, P. Hauke, J. Berges, and F. Jendrzejewski, *Science* **367**, 1128 (2020).
- [30] F. M. Surace, P. P. Mazza, G. Giudici, A. Lerose, A. Gambassi, and M. Dalmonte, “Lattice gauge theories and string dynamics in rydberg atom quantum simulators,” (2019), [arXiv:1902.09551](https://arxiv.org/abs/1902.09551).
- [31] B. Yang, H. Sun, R. Ott, H.-Y. Wang, T. V. Zache, J. C. Halimeh, Z.-S. Yuan, P. Hauke, and J.-W. Pan, “Observation of gauge invariance in a 71-site quantum simulator,” (2020), [arXiv:2003.08945](https://arxiv.org/abs/2003.08945).
- [32] R. Gerritsma, G. Kirchmair, F. Zähringer, E. Solano, R. Blatt, and C. F. Roos, *Nature* **463**, 68 (2010).
- [33] R. Gerritsma, B. P. Lanyon, G. Kirchmair, F. Zähringer,

- C. Hempel, J. Casanova, J. J. García-Ripoll, E. Solano, R. Blatt, and C. F. Roos, *Phys. Rev. Lett.* **106**, 060503 (2011).
- [34] E. A. Martinez, C. A. Muschik, P. Schindler, D. Nigg, A. Erhard, M. Heyl, P. Hauke, M. Dalmonte, T. Monz, P. Zoller, and R. Blatt, *Nature* **534**, 516 (2016).
- [35] E. Zohar, J. I. Cirac, and B. Reznik, *Reports on Progress in Physics* **79**, 014401 (2015).
- [36] M. Dalmonte and S. Montangero, *Contemporary Physics* **57**, 388 (2016).
- [37] M. C. Bañuls, R. Blatt, J. Catani, A. Celi, J. I. Cirac, M. Dalmonte, L. Fallani, K. Jansen, M. Lewenstein, S. Montangero, C. A. Muschik, B. Reznik, E. Rico, L. Tagliacozzo, K. V. Acoleyen, F. Verstraete, U. J. Wiese, M. Wingate, J. Zakrzewski, and P. Zoller, “Simulating lattice gauge theories within quantum technologies,” (2019), [arXiv:1911.00003](https://arxiv.org/abs/1911.00003).
- [38] M. Aidelsburger, L. Barbiero, A. Bermudez, T. Chanda, A. Dauphin, D. González-Cuadra, P. R. Grzybowski, S. Hands, F. Jendrzejewski, J. Jünemann, G. Juzeliunas, V. Kasper, A. Piga, S.-J. Ran, M. Rizzi, G. Sierra, L. Tagliacozzo, E. Tirrito, T. V. Zache, J. Zakrzewski, E. Zohar, and M. Lewenstein, “Cold atoms meet lattice gauge theory,” (2021), [arXiv:2106.03063](https://arxiv.org/abs/2106.03063) [[cond-mat.quant-gas](https://arxiv.org/abs/2106.03063)].
- [39] N. Klco, A. Roggero, and M. J. Savage, “Standard model physics and the digital quantum revolution: Thoughts about the interface,” (2021), [arXiv:2107.04769](https://arxiv.org/abs/2107.04769) [[quant-ph](https://arxiv.org/abs/2107.04769)].
- [40] V. A. Kostelecký and N. Russell, *Rev. Mod. Phys.* **83**, 11 (2011).
- [41] V. Galitski and I. B. Spielman, *Nature* **494**, 49 (2013).
- [42] L. Z. Liu, Xiong-Jun, L. Zhang, I. C. f. Q. Materials, and X.-J. Liu, “Chapter 1: Spin-orbit coupling and topological phases for ultracold atoms,”.
- [43] E. Dagotto, *Reports on Progress in Physics* **62**, 1525 (1999).
- [44] E. Dagotto and T. M. Rice, *Science* **271**, 618 (1996).
- [45] G. Sierra, *Journal of Physics A: Mathematical and General* **29**, 3299 (1996).
- [46] F. Haldane, *Physics Letters A* **93**, 464 (1983).
- [47] I. Affleck, *Nuclear Physics B* **257**, 397 (1985).
- [48] P. W. Anderson, *Phys. Rev.* **79**, 350 (1950).
- [49] J. Hubbard, *Proc. R. Soc. London, Ser. A* **276**, 238 (1963).
- [50] M. Fabrizio, *Phys. Rev. B* **48**, 15838 (1993).
- [51] L. Balents and M. P. A. Fisher, *Phys. Rev. B* **53**, 12133 (1996).
- [52] H.-H. Lin, L. Balents, and M. P. A. Fisher, *Phys. Rev. B* **58**, 1794 (1998).
- [53] H.-H. Lin, L. Balents, and M. P. A. Fisher, *Phys. Rev. B* **56**, 6569 (1997).
- [54] T. Giamarchi, *Quantum physics in one dimension*, Internat. Ser. Mono. Phys. (Clarendon Press, Oxford, 2004).
- [55] R. Noack, S. White, and D. Scalapino, *Physica C: Superconductivity* **270**, 281 (1996).
- [56] S. R. White, R. M. Noack, and D. J. Scalapino, *Phys. Rev. Lett.* **73**, 886 (1994).
- [57] S. R. White, *Phys. Rev. Lett.* **69**, 2863 (1992).
- [58] U. Schollwöck, *Rev. Mod. Phys.* **77**, 259 (2005).
- [59] K. v. Klitzing, G. Dorda, and M. Pepper, *Phys. Rev. Lett.* **45**, 494 (1980).
- [60] D. C. Tsui, H. L. Stormer, and A. C. Gossard, *Phys. Rev. Lett.* **48**, 1559 (1982).
- [61] R. Peierls, *Zeitschrift für Physik* **80**, 763 (1933).
- [62] G. Roux, E. Orignac, S. R. White, and D. Poilblanc, *Phys. Rev. B* **76**, 195105 (2007).
- [63] B. N. Narozhny, S. T. Carr, and A. A. Nersisyan, *Phys. Rev. B* **71**, 161101 (2005).
- [64] S. T. Carr, B. N. Narozhny, and A. A. Nersisyan, *Phys. Rev. B* **73**, 195114 (2006).
- [65] R. Jackiw and C. Rebbi, *Phys. Rev. D* **13**, 3398 (1976).
- [66] W. P. Su, J. R. Schrieffer, and A. J. Heeger, *Phys. Rev. Lett.* **42**, 1698 (1979).
- [67] R. Jackiw and J. Schrieffer, *Nuclear Physics B* **190**, 253 (1981).
- [68] M. Atala, M. Aidelsburger, M. Lohse, J. T. Barreiro, B. Paredes, and I. Bloch, *Nature Physics* **10**, 588 (2014).
- [69] M. E. Tai, A. Lukin, M. Rispoli, R. Schittko, T. Menke, D. Borgnia, P. M. Preiss, F. Grusdt, A. M. Kaufman, and M. Greiner, *Nature* **546**, 519 (2017).
- [70] M. P. A. Fisher, P. B. Weichman, G. Grinstein, and D. S. Fisher, *Phys. Rev. B* **40**, 546 (1989).
- [71] D. Jaksch, C. Bruder, J. I. Cirac, C. W. Gardiner, and P. Zoller, *Phys. Rev. Lett.* **81**, 3108 (1998).
- [72] E. Orignac and T. Giamarchi, *Phys. Rev. B* **64**, 144515 (2001).
- [73] D. Hülgel and B. Paredes, *Phys. Rev. A* **89**, 023619 (2014).
- [74] A. Petrescu and K. Le Hur, *Phys. Rev. Lett.* **111**, 150601 (2013).
- [75] M. Piraud, F. Heidrich-Meisner, I. P. McCulloch, S. Greschner, T. Vekua, and U. Schollwöck, *Phys. Rev. B* **91**, 140406 (2015).
- [76] A. Dhar, T. Mishra, M. Maji, R. V. Pai, S. Mukerjee, and A. Paramekanti, *Phys. Rev. B* **87**, 174501 (2013).
- [77] S. Greschner, M. Piraud, F. Heidrich-Meisner, I. P. McCulloch, U. Schollwöck, and T. Vekua, *Phys. Rev. Lett.* **115**, 190402 (2015).
- [78] R. B. Laughlin, *Phys. Rev. Lett.* **50**, 1395 (1983).
- [79] E. Cornfeld and E. Sela, *Phys. Rev. B* **92**, 115446 (2015).
- [80] M. Calvanese Strinati, E. Cornfeld, D. Rossini, S. Barbarino, M. Dalmonte, R. Fazio, E. Sela, and L. Mazza, *Phys. Rev. X* **7**, 021033 (2017).
- [81] M. Creutz, *Phys. Rev. Lett.* **83**, 2636 (1999).
- [82] M. Creutz, *Rev. Mod. Phys.* **73**, 119 (2001).
- [83] D. B. Kaplan, *Physics Letters B* **288**, 342 (1992).
- [84] K. Jansen and M. Schmaltz, *Physics Letters B* **296**, 374 (1992).
- [85] M. F. Golterman, K. Jansen, and D. B. Kaplan, *Physics Letters B* **301**, 219 (1993).
- [86] D. B. Kaplan, in *Les Houches Summer School: Session 93: Modern perspectives in lattice QCD: Quantum field theory and high performance computing* (2009) pp. 223–272, [arXiv:0912.2560](https://arxiv.org/abs/0912.2560) [[hep-lat](https://arxiv.org/abs/0912.2560)].
- [87] J. B. Kogut, *Rev. Mod. Phys.* **51**, 659 (1979).
- [88] J. B. Kogut, *Rev. Mod. Phys.* **55**, 775 (1983).
- [89] D. Leykam, A. Andreanov, and S. Flach, *Advances in Physics: X* **3**, 1473052 (2018).
- [90] J. Vidal, R. Mosseri, and B. Douçot, *Phys. Rev. Lett.* **81**, 5888 (1998).
- [91] L. Mazza, A. Bermudez, N. Goldman, M. Rizzi, M. A. Martin-Delgado, and M. Lewenstein, *New Journal of Physics* **14**, 015007 (2012).
- [92] C. G. Velasco and B. Paredes, “Classification of topological ladder models,” (2019), [arXiv:1907.11460](https://arxiv.org/abs/1907.11460).
- [93] O. Viyuela, A. Rivas, and M. A. Martin-Delgado, *Phys. Rev. B* **86**, 155140 (2012).
- [94] O. Viyuela, A. Rivas, and M. A. Martin-Delgado, *Phys. Rev. Lett.* **112**, 130401 (2014).
- [95] A. Bermudez, D. Patanè, L. Amico, and M. A. Martin-Delgado, *Phys. Rev. Lett.* **102**, 135702 (2009).
- [96] R. Jafari, H. Johannesson, A. Langari, and M. A. Martin-Delgado, *Phys. Rev. B* **99**, 054302 (2019).
- [97] N. Sun and L.-K. Lim, *Phys. Rev. B* **96**, 035139 (2017).
- [98] S. D. Huber and E. Altman, *Phys. Rev. B* **82**, 184502 (2010).
- [99] S. Takayoshi, H. Katsura, N. Watanabe, and H. Aoki, *Phys.*

- Rev. A* **88**, 063613 (2013).
- [100] M. Tovmasyan, E. P. L. van Nieuwenburg, and S. D. Huber, *Phys. Rev. B* **88**, 220510 (2013).
- [101] H. Alaeian, C. W. S. Chang, M. V. Mghaddam, C. M. Wilson, E. Solano, and E. Rico, *Phys. Rev. A* **99**, 053834 (2019).
- [102] J. Zurita, C. E. Creffield, and G. Platero, *Advanced Quantum Technologies* **3**, 1900105 (2020).
- [103] Y. He, R. Mao, H. Cai, J.-X. Zhang, Y. Li, L. Yuan, S.-Y. Zhu, and D.-W. Wang, *Phys. Rev. Lett.* **126**, 103601 (2021).
- [104] S. Rachel, *Reports on Progress in Physics* **81**, 116501 (2018).
- [105] N. B. Kopnin, T. T. Heikkilä, and G. E. Volovik, *Phys. Rev. B* **83**, 220503 (2011).
- [106] S. Peotta and P. Törmä, *Nature Communications* **6**, 8944 (2015).
- [107] M. Tovmasyan, S. Peotta, P. Törmä, and S. D. Huber, *Phys. Rev. B* **94**, 245149 (2016).
- [108] M. Tovmasyan, S. Peotta, L. Liang, P. Törmä, and S. D. Huber, *Phys. Rev. B* **98**, 134513 (2018).
- [109] R. Mondaini, G. G. Batrouni, and B. Grémaud, *Phys. Rev. B* **98**, 155142 (2018).
- [110] D. Sticlet, L. Seabra, F. Pollmann, and J. Cayssol, *Phys. Rev. B* **89**, 115430 (2014).
- [111] Y. Kuno, T. Orito, and I. Ichinose, *New Journal of Physics* **22**, 013032 (2020).
- [112] C. Danieli, A. Andreanov, and S. Flach, *Phys. Rev. B* **102**, 041116 (2020).
- [113] R. Nandkishore and D. A. Huse, *Annual Review of Condensed Matter Physics* **6**, 15 (2015).
- [114] O. Boada, A. Celi, J. I. Latorre, and M. Lewenstein, *Phys. Rev. Lett.* **108**, 133001 (2012).
- [115] A. Celi, P. Massignan, J. Ruseckas, N. Goldman, I. B. Spielman, G. Juzeliūnas, and M. Lewenstein, *Phys. Rev. Lett.* **112**, 043001 (2014).
- [116] T. Ozawa and H. M. Price, *Nature Reviews Physics* **1**, 349 (2019).
- [117] M. Mancini, G. Pagano, G. Cappellini, L. Livi, M. Rider, J. Catani, C. Sias, P. Zoller, M. Inguscio, M. Dalmonte, and L. Fallani, *Science* **349**, 1510 (2015), <https://science.sciencemag.org/content/349/6255/1510.full.pdf>.
- [118] B. K. Stuhl, H.-I. Lu, L. M. Ayccock, D. Genkina, and I. B. Spielman, *Science* **349**, 1514 (2015), <https://science.sciencemag.org/content/349/6255/1514.full.pdf>.
- [119] J. H. Han, J. H. Kang, and Y. Shin, *Phys. Rev. Lett.* **122**, 065303 (2019).
- [120] L. F. Livi, G. Cappellini, M. Diem, L. Franchi, C. Clivati, M. Frittelli, F. Levi, D. Calonico, J. Catani, M. Inguscio, and L. Fallani, *Phys. Rev. Lett.* **117**, 220401 (2016).
- [121] S. Kolkowitz, S. L. Bromley, T. Bothwell, M. L. Wall, G. E. Marti, A. P. Koller, X. Zhang, A. M. Rey, and J. Ye, *Nature* **542**, 66 (2017).
- [122] S. L. Bromley, S. Kolkowitz, T. Bothwell, D. Kedar, A. Safavi-Naini, M. L. Wall, C. Salomon, A. M. Rey, and J. Ye, *Nature Physics* **14**, 399 (2018).
- [123] A. V. Gorshkov, M. Hermele, V. Gurarie, C. Xu, P. S. Julienne, J. Ye, P. Zoller, E. Demler, M. D. Lukin, and A. M. Rey, *Nature Physics* **6**, 289 (2010).
- [124] G. Pagano, M. Mancini, G. Cappellini, P. Lombardi, F. Schäfer, H. Hu, X.-J. Liu, J. Catani, C. Sias, M. Inguscio, and L. Fallani, *Nature Physics* **10**, 198 (2014).
- [125] S. Barbarino, L. Taddia, D. Rossini, L. Mazza, and R. Fazio, *New Journal of Physics* **18**, 035010 (2016).
- [126] T. Bilitewski and N. R. Cooper, *Phys. Rev. A* **94**, 023630 (2016).
- [127] T. Y. Saito and S. Furukawa, *Phys. Rev. A* **95**, 043613 (2017).
- [128] L. Taddia, E. Cornfeld, D. Rossini, L. Mazza, E. Sela, and R. Fazio, *Phys. Rev. Lett.* **118**, 230402 (2017).
- [129] S. Barbarino, M. Dalmonte, R. Fazio, and G. E. Santoro, *Phys. Rev. A* **97**, 013634 (2018).
- [130] M. Calvanese Strinati, S. Sahoo, K. Shtengel, and E. Sela, *Phys. Rev. B* **99**, 245101 (2019).
- [131] J. Jünemann, A. Piga, S.-J. Ran, M. Lewenstein, M. Rizzi, and A. Bermudez, *Phys. Rev. X* **7**, 031057 (2017).
- [132] A. Eckardt, *Rev. Mod. Phys.* **89**, 011004 (2017).
- [133] J. Zak, *Phys. Rev. Lett.* **62**, 2747 (1989).
- [134] M. V. Berry, *Proceedings of the Royal Society of London. A. Mathematical and Physical Sciences* **392**, 45 (1984).
- [135] A. P. Schnyder, S. Ryu, A. Furusaki, and A. W. W. Ludwig, *Phys. Rev. B* **78**, 195125 (2008).
- [136] A. Kitaev, *AIP Conference Proceedings* **1134**, 22 (2009).
- [137] S. A. Parameswaran, R. Roy, and S. L. Sondhi, *Comptes Rendus Physique* **14**, 816 (2013), topological insulators / Isolants topologiques.
- [138] K. G. Wilson, in *New Phenomena in Subnuclear Physics* (Springer US, 1977) pp. 69–142.
- [139] D. J. Gross and A. Neveu, *Phys. Rev. D* **10**, 3235 (1974).
- [140] E. Fermi, *Zeitschrift für Physik* **88**, 161 (1934).
- [141] F. L. Wilson, *American Journal of Physics* **36**, 1150 (1968).
- [142] A. Bermudez, E. Tirrito, M. Rizzi, M. Lewenstein, and S. Hands, *Annals of Physics* **399**, 149 (2018).
- [143] E. Tirrito, M. Rizzi, G. Sierra, M. Lewenstein, and A. Bermudez, *Phys. Rev. B* **99**, 125106 (2019).
- [144] A. Hamed Moosavian and S. Jordan, *Phys. Rev. A* **98**, 012332 (2018).
- [145] D.-S. Li, H. Wang, C. Guo, M. Zhong, and P.-X. Chen, “Simulation of state evolutions in gross-neveu model by matrix product state representation,” (2020), [arXiv:2011.07538 \[hep-th\]](https://arxiv.org/abs/2011.07538).
- [146] A. M. Czajka, Z.-B. Kang, H. Ma, and F. Zhao, “Quantum simulation of chiral phase transitions,” (2021), [arXiv:2112.03944 \[hep-ph\]](https://arxiv.org/abs/2112.03944).
- [147] S. Aoki, *Phys. Rev. D* **30**, 2653 (1984).
- [148] S. Sharpe and R. Singleton, *Phys. Rev. D* **58**, 074501 (1998).
- [149] D. B. Kaplan, “Chiral symmetry and lattice fermions,” (2012), [arXiv:0912.2560 \[hep-lat\]](https://arxiv.org/abs/0912.2560).
- [150] W. Sun, B.-Z. Wang, X.-T. Xu, C.-R. Yi, L. Zhang, Z. Wu, Y. Deng, X.-J. Liu, S. Chen, and J.-W. Pan, *Phys. Rev. Lett.* **121**, 150401 (2018).
- [151] B. Song, L. Zhang, C. He, T. F. J. Poon, E. Hajiyeve, S. Zhang, X.-J. Liu, and G.-B. Jo, *Science* **360**, 4748 (2018), [10.1126/sciadv.aao4748](https://doi.org/10.1126/sciadv.aao4748).
- [152] Z. Wu, L. Zhang, W. Sun, X.-T. Xu, B.-Z. Wang, S.-C. Ji, Y. Deng, S. Chen, X.-J. Liu, and J.-W. Pan, *Science* **354**, 83 (2016).
- [153] M.-C. Liang, Y.-D. Wei, L. Zhang, X.-J. Wang, H. Zhang, W.-W. Wang, W. Qi, X.-J. Liu, and X. Zhang, “Realization of qi-wu-zhang model in spin-orbit-coupled ultracold fermions,” (2021), [arXiv:2109.08885 \[cond-mat.quant-gas\]](https://arxiv.org/abs/2109.08885).
- [154] H. Nielsen and M. Ninomiya, *Nuclear Physics B* **185**, 20 (1981).
- [155] H. Nielsen and M. Ninomiya, *Nuclear Physics B* **193**, 173 (1981).
- [156] N. Manton, *Annals of Physics* **159**, 220 (1985).
- [157] J. Ambjorn, J. Greensite, and C. Peterson, *Nuclear Physics B* **221**, 381 (1983).
- [158] L. Fu, *Physical Review Letters* **106**, 106802 (2011).
- [159] Y. Ando and L. Fu, *Annu. Rev. Condens. Matter Phys.* **6**, 361 (2015).
- [160] H. Isobe and L. Fu, *Physical Review B* **92**, 081304 (2015).
- [161] E. Lieb, T. Schultz, and D. Mattis, *Annals of Physics* **16**, 407 (1961).

- [162] E. Barouch and B. M. McCoy, *Phys. Rev. A* **3**, 786 (1971).
- [163] T. Moriya, *Phys. Rev.* **120**, 91 (1960).
- [164] I. Dzyaloshinsky, *Journal of Physics and Chemistry of Solids* **4**, 241 (1958).
- [165] P. Jordan and E. Wigner, *Zeitschrift für Physik* **47**, 631 (1928).
- [166] N. N. Bogoljubov, *Il Nuovo Cimento (1955-1965)* **7**, 794 (1958).
- [167] H. Bruus and K. Flensberg, *Many-body quantum theory in condensed matter physics: an introduction* (Oxford University Press, 2017).
- [168] P. Coleman, *Introduction to Many-Body Physics* (Cambridge University Press, 2015).
- [169] M. C. Bañuls and K. Cichy, *Reports on Progress in Physics* **83**, 024401 (2020).
- [170] F. Pollmann, A. M. Turner, E. Berg, and M. Oshikawa, *Phys. Rev. B* **81**, 064439 (2010).
- [171] M. B. Plenio and S. S. Virmani, *Quantum information and coherence*, 173 (2014).
- [172] L. Amico, R. Fazio, A. Osterloh, and V. Vedral, *Reviews of modern physics* **80**, 517 (2008).
- [173] H. Li and F. D. M. Haldane, *Physical review letters* **101**, 010504 (2008).
- [174] F. Pollmann, A. M. Turner, E. Berg, and M. Oshikawa, *Physical review b* **81**, 064439 (2010).
- [175] L. Fidkowski, *Physical review letters* **104**, 130502 (2010).
- [176] F. Pollmann, E. Berg, A. M. Turner, and M. Oshikawa, *Physical review b* **85**, 075125 (2012).
- [177] G. Vidal, J. I. Latorre, E. Rico, and A. Kitaev, *Physical review letters* **90**, 227902 (2003).
- [178] P. Calabrese and J. Cardy, *Journal of statistical mechanics: theory and experiment* **2004**, P06002 (2004).
- [179] P. Calabrese and J. Cardy, *Journal of physics a: mathematical and theoretical* **42**, 504005 (2009).
- [180] I. Bloch, J. Dalibard, and W. Zwerger, *Rev. Mod. Phys.* **80**, 885 (2008).
- [181] J. H. Kang, J. H. Han, and Y. Shin, *Phys. Rev. Lett.* **121**, 150403 (2018).
- [182] J. H. Kang, J. H. Han, and Y. Shin, *New Journal of Physics* **22**, 013023 (2020).
- [183] W. Hofstetter, J. I. Cirac, P. Zoller, E. Demler, and M. D. Lukin, *Phys. Rev. Lett.* **89**, 220407 (2002).
- [184] M. Mancini *et al.*, *Science* **349**, 1510 (2015), [arXiv:1502.02495 \[cond-mat.quant-gas\]](https://arxiv.org/abs/1502.02495).
- [185] B. K. Stuhl, H.-I. Lu, L. M. Ayccock, D. Genkina, and I. B. Spielman, *Science* **349**, 1514–1518 (2015).
- [186] D. Jaksch and P. Zoller, *New Journal of Physics* **5**, 56 (2003).
- [187] M. Reitter, J. Näger, K. Wintersperger, C. Sträter, I. Bloch, A. Eckardt, and U. Schneider, *Phys. Rev. Lett.* **119**, 200402 (2017).
- [188] K. Wintersperger, M. Bukov, J. Näger, S. Lellouch, E. Demler, U. Schneider, I. Bloch, N. Goldman, and M. Aidelsburger, *Phys. Rev. X* **10**, 011030 (2020).
- [189] W. Xu, W. Morong, H.-Y. Hui, V. W. Scarola, and B. DeMarco, *Phys. Rev. A* **98**, 023623 (2018).
- [190] M. Messer, K. Sandholzer, F. Görg, J. Minguzzi, R. Desbuquois, and T. Esslinger, *Phys. Rev. Lett.* **121**, 233603 (2018).
- [191] F. Görg, K. Sandholzer, J. Minguzzi, R. Desbuquois, M. Messer, and T. Esslinger, *Nature Physics* **15**, 1161 (2019).
- [192] K. Viebahn, J. Minguzzi, K. Sandholzer, A.-S. Walter, M. Sajani, F. Görg, and T. Esslinger, *Phys. Rev. X* **11**, 011057 (2021).
- [193] X.-J. Liu, Z.-X. Liu, and M. Cheng, *Phys. Rev. Lett.* **110**, 076401 (2013).
- [194] X.-J. Liu, K. T. Law, and T. K. Ng, *Phys. Rev. Lett.* **112**, 086401 (2014).
- [195] X.-J. Liu, K. T. Law, and T. K. Ng, *Phys. Rev. Lett.* **113**, 059901 (2014).
- [196] L. Ziegler, E. Tirrito, M. Lewenstein, S. Hands, and A. Bermudez, “Correlated chern insulators in two-dimensional raman lattices: a cold-atom regularization of strongly-coupled four-fermi field theories,” (2020), [arXiv:2011.08744 \[cond-mat.quant-gas\]](https://arxiv.org/abs/2011.08744).
- [197] L. Ziegler, E. Tirrito, M. Lewenstein, S. Hands, and A. Bermudez, “Large- n chern insulators: lattice field theory and quantum simulation approaches to correlation effects in the quantum anomalous hall effect,” (2021), [arXiv:2111.04485 \[cond-mat.quant-gas\]](https://arxiv.org/abs/2111.04485).
- [198] F. Gerbier and J. Dalibard, *New Journal of Physics* **12**, 033007 (2010).
- [199] N. Q. Burdick, Y. Tang, and B. L. Lev, *Phys. Rev. X* **6**, 031022 (2016).
- [200] B. Song, C. He, S. Zhang, E. Hajiyev, W. Huang, X.-J. Liu, and G.-B. Jo, *Phys. Rev. A* **94**, 061604 (2016).
- [201] D. González-Cuadra, L. Tagliacozzo, M. Lewenstein, and A. Bermudez, *Phys. Rev. X* **10**, 041007 (2020).
- [202] G. Magnifico, D. Vodola, E. Ercolessi, S. P. Kumar, M. Müller, and A. Bermudez, *Phys. Rev. D* **99**, 014503 (2019).
- [203] G. Magnifico, D. Vodola, E. Ercolessi, S. P. Kumar, M. Müller, and A. Bermudez, *Phys. Rev. B* **100**, 115152 (2019).
- [204] P. Jordan and E. P. Wigner, in *The Collected Works of Eugene Paul Wigner* (Springer, 1993) pp. 109–129.